UNIVERSITY OF OTTAWA

DEPARTMENT OF MECHANICAL ENGINEERING

Modelling and Simulation of the Nonlinear Dynamics of Arrays of Coupled Filaments for Robot Walkers

Author:
Keeragala Gunasingha

Supervisor:
Davide Spinello

A thesis submitted in partial fulfillment of the requirements for the degree in

Master of Science Systems Science

uOttawa

Abstract

This thesis project centers on modelling and simulation of the nonlinear dynamics of systems of filaments attached to a solid substrate that couples their motion. The geometry of the system is inspired by ubiquitous structures found in small organisms. These structures, called cilia, exhibit different types of organized coordinated patterns used for locomotion, among other functions. One notable type of coordination is called metachronal, which manifests through wave propagation across the filaments, and it is inherently related to motility and locomotion. The same type of wave phenomena are observed in larger organisms such as centipedes and millipedes, which use it for terrestrial locomotion. While there are many studies on cilia-inspired robot locomotion, they often focus on hydrodynamic coupling or magnetic actuation. This thesis introduces a model with mechanical coupling.

The main objective of the thesis is to derive a mechanical model and to simulate it, creating the foundation for the systematic prediction of the emergence of coordinated patterns of the system. The ultimate goal for future work is to use the predictions to design controls for terrestrial locomotion systems for mobile autonomous robots capable of navigating across various terrains.

The system we simulate consists of arrays of rigid filaments that are coupled through visco-elastic lumped elements at the base. These filaments emulate hair-like structures idealized as inverted pendulums, capturing certain characteristics of cilia-like structures that are relevant for the locomotion. Mechanical coupling is achieved through elastic springs and linear viscous dampers, creating a lumped-parameter model of the coupling base. The governing equations for the system are derived using Euler-Lagrange's formalism.

In simulations, our primary objective is to examine coordinated patterns under diverse initial conditions. The evolution of the simulated system demonstrates a convergence towards a synchronized state. The study contributes to the exploration of bio-inspired approaches for developing robust terrestrial robot walkers capable of adaptive and efficient movement.

Dedication

This work is dedicated to the unwavering love and support of my family. To my beloved husband, whose encouragement and understanding have been my anchor throughout this journey. To my wonderful son, whose laughter and presence have brought joy to even the most challenging days.

To my parents, though distance separates us, your sacrifices and belief in me have illuminated my path. This achievement is a tribute to your enduring love and unwavering faith.

Acknowledgments

I would like to extend my heartfelt appreciation to Dr. Davide Spinello, my supervisor, for his invaluable mentorship and tireless dedication. His expertise, encouragement, and insightful feedback have played a pivotal role in shaping the course of this research.

I also wish to express my gratitude to my committee members, namely Dr. Thomas Uchida and Dr. Mohammad Pirani. I deeply appreciate their generous commitment to reviewing my thesis.

Furthermore, I want to acknowledge the unwavering encouragement from my parents, my husband, and my son in my pursuit of my passions, whatever they may be.

Last but not least, I am also deeply grateful to all the mentors, advisors, and sources of knowledge that have contributed to the development of my research. Your wisdom has equipped me with the tools necessary to explore new horizons.

This achievement stands as a testament to the collective efforts of these exceptional individuals, and I am truly honored to have them as a part of my life.

Contents

List of Figures

List of Tables

Chapter 1

Introduction

Terrestrial robot walkers are a class of robotic devices designed to move on ground, often by mimicking the walking patterns of animals or humans. Many terrestrial robot walkers are inspired by the locomotion of animals or insects, and their designs may be based on the biomechanics of specific creatures [1][2]. Different designs have been proposed, with distinct advantages based on the applications [3]. Wheeled robots, characterized by their primary wheel-based locomotion, excel in stability and efficiency on flat surfaces. In contrast, legged terrestrial robots, capable of walking, crawling, and climbing, exhibit versatility [4][5]. The number of legs can vary, with implications for stability and control complexity. As the number of legs increases, the robot's stability improves, but the complexity of the control system also increases [4].

Many invertebrate animals employ a unique locomotion strategy known as 'travelling deformations' or waves along their bodies [6]. This continuous, wave-like motion enables them to navigate complex environments without the risk of becoming stuck, a limitation often associated with limbs and wheels. These animals achieve this wave-like movement by sequentially activating distinct sections along their bodies in a coordinated sequence, known as a 'metachronal wave', which is a type of travelling wave pattern often observed in biological systems [6][7].

In the development of robots, leveraging metachronal coordination can lead to viable and robust terrestrial locomotion systems [8]. The use of flexible filaments employed in the construction of robotic legs, in tandem with precise coordination, can be a viable approach for terrestrial locomotion, requiring proper actuation to induce the necessary coordinated patterns. This biomimetic approach, inspired by the metachronal wave observed in invertebrates, holds promise for enhancing the adaptability and efficiency of robotic locomotion in diverse and challenging environments [9][8].

1.1 Motivation and Inspiration

The development of bio-inspired robotic techniques represents a pathway to more efficient, adaptable, and versatile robotic solutions with a wide range of real-world applications [10].

Developing novel bio-inspired robotic techniques not only opens up new possibilities for previously unattainable applications, but also deepens our understanding of biomechanics and physiology. By mimicking biological structures and functions, researchers gain insight into human and animal locomotion and manipulation [2][10].

Exploring coordination in robotic locomotion is significant for a variety of reasons. Coordinated movement can lead to more efficient and optimized robot performance, saving time and resources [11]. Collective motions allow organisms to adapt to evolving environments and navigate through complex and unpredictable terrains [10]. Robots that can mimic such behaviour can be more robust and adaptable, making them suitable for various real-world scenarios, from disaster response to search and rescue missions. Researching collective motion in robots can also advance our fundamental understanding of complex systems and the principles governing collective behaviour [8][9].

This thesis draws inspiration from the movement of certain microorganisms and small organisms that employ cilia for propulsion [8]. It aims at modelling a locomotion mechanism for terrestrial robot walkers based on these phenomena. Cilia are small hair-like flexible structures that extend from the surfaces of eukaryotic cells [12]. Cilia interact with a surrounding fluid primarily to generate thrust for locomotion and motility. Cilia help to move small particles in the fluid. For example, in the respiratory tract, cilia move mucus and trapped particles out of the lungs. Moreover, cilia are adept at transporting various substances through the fluid environment. This can include the movement of nutrients, signaling molecules, or waste products. In some cases, cilia can be involved in the propulsion of the cell itself [7][13][14]. Designing robot appendages that resemble cilia-like structures can be a starting point for creating a terrestrial robot capable of navigating diverse terrains [15]. These appendages are thin and flexible, able to bend and move in a coordinated manner to produce propulsion [15]. When cilia are coupled in large groups, they exhibit coordinated motions, leading to emergent synchronization. The synchronized motion in which the protrusions move with constant phase difference among contiguous ones is known as metachronal coordination, and it is especially relevant for locomotion [7].

The essential characteristics of cilia arrays, including alignment, individual filament movements, and metachronal coordination, can serve as the foundation for designing a robot locomotion system [16]. The metachronal coordination, representing the sequential beating of cilia, plays a pivotal role in generating forward propulsion. By replicating the direction and timing of cilia beats, the robot can move through rhythmic motions, effectively propelling itself forward [17][7]. This biomimetic approach goes beyond simple replication of aquatic phenomena by systematically transferring fundamental principles into non-aquatic environments. There are terrestrial animals, like millipedes, that use metachronal coordination. The fundamental problem is that modelling is mostly done for aquatic locomotion, since terrestrial locomotion requires different mathematical treatment, as the coupling is not overdamped. The objective of this thesis is to capitalize on the intrinsic efficiency of aquatic locomotion and integrate these principles into the design of robotic systems, thereby achieving optimal and smooth terrestrial movement [9][18].

1.2 Thesis Objectives and Contributions

The objectives of this thesis can be summarized as follows:

- Modelling a system consisting of two-dimensional arrays of mechanically coupled oscillators, representing a set of legs for terrestrial walking robots.
- Simulating the dynamics of the system to obtain some insight about emergence of coordinate patterns such as synchronization, phase-locked state or metachronal waves.
- From the result, recommend future directions of investigation towards the design of controls and actuations to induce coordinated patterns for walking and robot locomotion.

Our work is dedicated to developing a model tailored for a specific class of robotic devices, particularly miniature robots designed for hazardous environments. This study serves as a preliminary exploration into the coordinated patterns of such systems, introducing a visco-elastic model.

The contribution of work can be summarized as follows:

- Using a Lagrangian approach to model a complex nonlinear mechanical system that is the basis for a bio-inspired locomotion system for terrestrial robots.
- In simulation, investigating the emergence of coordinated patterns of the system's variables that are relevant for the design of miniature terrestrial locomotion systems.

- The parameters, including leg length and mass, are adaptable for different robotic devices. Adjusting the stiffness and damping parameters is critical for optimizing performance in various environments.

Further development will involve extending these findings to explore behaviour across various environments, a crucial step in enhancing the adaptability and performance of these robots.

1.3 Thesis Outline

The thesis is outlined as follows:

Chapter 1 serves as the introduction, where I explain the key aspects of the thesis. It outlines the thesis objective, draws inspiration from cilia with their coordinated beating patterns, and highlights the contributions made in exploring potential solutions for terrestrial robot locomotion.

Chapter 2 provides a thorough examination of the significance of bio-inspired robotic walkers. It delves into existing literature that explores cilia beating patterns in hydrodynamic interactions and magnetic coupling. Additionally, the chapter discusses relevant theories related to model equations, offering an overview of the foundational concepts and research in this field.

Chapter 3 provides a detailed exposition of the methodology employed in formulating the model and deriving the equations of motion. Our system comprises arrays of rigid filaments with visco-elastic coupling through a basis. The filaments are represented as hair-like structures resembling inverted pendulums, reproducing some relevant characteristics of cilia. Elastic springs and linear viscous dampers mechanically couple the filaments, representing a lumped-parameter model of the coupling base. Euler-Lagrange's equation allows us to derive the governing equations.

Chapter 4 presents the results obtained through numerical simulations of the model under various conditions and parameter settings. The parameters are determined by considering the scale of designing miniature terrestrial robots for hazardous environments capable of navigating diverse terrains. However, the proposed model is flexible, allowing for adjustments in parameters. In simulations, the goal is to predict the emergence of coordination patterns that are applicable to robot design. This observation indicates the potential for designing effective locomotion mechanisms based on these coordinated patterns. For reference, the simulation code used is provided in Appendix A.

Chapter 5 offers a comprehensive summary of the findings presented in this study and future work.

Chapter 2

Literature Review

2.1 Terrestrial Robots

Terrestrial robots, specifically designed for operation on solid ground, offer a diverse set of applications across various industries. These robots serve crucial roles in manufacturing, agriculture, construction, search and rescue missions, healthcare, and more. Terrestrial robots come in several distinct forms, each tailored to particular tasks and environments. These include wheeled robots, legged robots, multi-legged robots, crawler robots, soft robots, and autonomous vehicles, among various other types [19][20][21].

Wheeled robots are characterized by their use of wheels or tracks for mobility, making them efficient and suitable for flat and smooth surfaces [5]. These robots excel in high-speed and energy-efficient tasks, commonly finding applications indoors, such as in warehouses and factories. However, they face challenges when encountering obstacles or stairs, limiting their adaptability to changing environments [22].

In contrast, legged robots are generally suitable in rough and uneven terrain, having the capability to traverse obstacles and climb stairs [5]. Their versatility extends to various applications, including exploration and search and rescue missions. Nevertheless, legged robots require complex control systems for stable locomotion and tend to operate at slower speeds compared to wheeled counterparts, resulting in higher energy consumption [23][24].

A bipedal walking robot is a type of humanoid robot designed to imitate human movement [1], specifically focused on walking on two legs [25]. Humanoid robots, on the other hand, covers a wider range of designs. As an example, Miwa et al. demonstrated humanoid robots with only an upper body or a head [25]. Over decades of development, humanoid robots have progressed significantly, not only gaining the ability to walk, run, and jump, but also achieving movement on irregular ground. One of the key advantages of humanoid robots lies in their adaptability to diverse and complex environments, such as navigating narrow passages, stairs, and various rugged terrains. Moreover, they can directly utilize tools designed for humans. The evolution of humanoid robots has also seen the integration of both wheeled and legged mechanisms. This combination allows robots to attain higher moving speeds and larger moving ranges. ETH Zurich's Ascento serves as an illustration of a small wheel-legged jumping robot, showcasing quick movement on flat terrain and the ability to overcome obstacles through jumping [26].

Multilegged robots, equipped with multiple legs, often six or more, prioritize stability and load-bearing capabilities. These robots are particularly suitable in tasks demanding precise positioning and manipulation across diverse terrains, particularly in heavy-duty applications. However, their complex mechanical design and control systems lead to slower operation compared to wheeled robots, and maintenance and repair can pose challenges due to the presence of multiple moving parts [23][19].

Soft robots, often bio-inspired, incorporate soft or compliant components within their mechanical structures, drawing insights from organisms like octopuses and caterpillars [27]. Soft robots deploy soft, compliant materials and flexible actuation techniques to replicate the adaptability and locomotion observed in nature [28]. They find applications in diverse fields, including search and rescue, exploration, and precision tasks [29]. Soft robotics, however, presents unique challenges related to control, modelling, and materials [27].

In summary, terrestrial robots encompass a spectrum of forms, each with its unique advantages and limitations, enabling them to perform critical roles in a wide range of industries and applications. Among the various types of robots, our focus is specifically on studying coordinated leg movements in multi-legged robots.

2.1.1 Biomechanics-Inspired Locomotion in Multi-Legged Robots

Biomimetic or bio-robots are designed and developed by drawing inspiration from biological organisms, their structures, behaviours, and mechanisms [19][2]. Biological organisms have evolved over millions of years to be highly efficient and adaptable to their environments. By mimicking their designs and behaviours, researchers can address challenges in robotics, such as locomotion in challenging terrains, navigation, and manipulation of objects [2]

These robots have the potential for various applications, and research focuses on enhancing their stability, speed, and adaptability. Some robots aim to mimic the locomotion

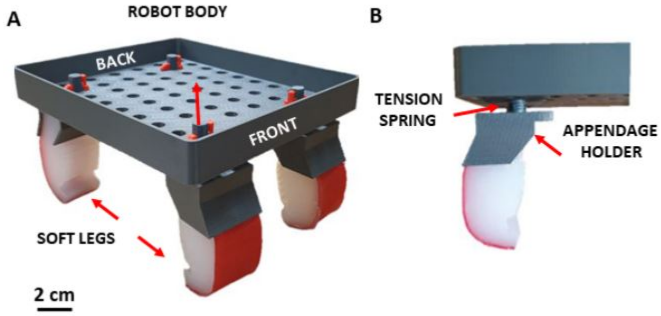

Figure 2.1: Modular, soft-legged quadruped robot. A. The robot consists of a perforated, rectangular, 3D-printed body part and four fabric-reinforced, soft legs. B. Soft legs that are attached to the perforated body via a spring latch mechanism. Used with permission of ref. [30]; letter attached in Appendix A.

patterns of animals like insects, involving coordinated leg movements for efficient motion [2].

Siddiquee et al. designed a hybrid modular quadruped robot that draws inspiration from biological systems [30]. The paper introduces a soft modular appendage crafted from silicone that is powered by pneumatic mechanisms. The robot described in the study features four identical soft legs, as illustrated in Figure 2.1. The connection of the soft legs to the rigid body is facilitated by appendage holders that are affixed to the body using a spring-latch mechanism. This mechanism comprises a tension spring and a connector key, which securely fastens the leg to the body. Importantly, the cylindrical shape of the upper portion of the appendage holder permits the appendages to rotate about the vertical axis. This flexibility allows for alterations in the robot's shape, enabling it to adapt effectively to various environments and perform different tasks as needed. The study identified certain limitations. These limitations primarily pertain to manufacturing errors associated with the soft appendages.

Ruomeng Xu and Qingsong Xu discuss the development of soft robots inspired by natural insect locomotion patterns, with a particular focus on a novel soft octopodal robot designed for potential biomedical applications [31]. The paper presents a soft octopodal robot, designed to meet the demands of biomedical environments. The locomotion is achieved by magnetizing the soft robot through the incorporation of magnetic particles into silicone polymers. The prototypes of the soft robot are fabricated by mixing magnetic particles with silicone polymers and subsequently magnetized using a specific magnetic field. These robots are actuated by an external magnetic field generated by custom-made electromagnetic coils, with a magnetic field strength in the range of 5–8 mT. Experiments demonstrate that the robot achieves high speeds, ranging from 0.536 to 1.604 mm/s, on various surfaces, including paper, wood, and PMMA (polymethyl methacrylate). Importantly, these speeds are achieved with relatively low magnetic field strength, leading to energy-efficient locomotion.

Addressing challenges is crucial for legged robots, contributing to overall performance and stability, especially in the context of navigating natural terrains. Controlling walking robots involves planning specific attributes of the desired gait, simplifying the complexity of motion planning while simultaneously enhancing performance, safety, and stability [16][32].

Walkers can achieve either static or dynamic stability [16][33]. In the case of static stability, the robot remains in a state of static equilibrium throughout its movement [16]. This implies that the robot is constantly supported by a minimum of three contact points, and these points encompass the robot's center of gravity. To achieve static stability, robots typically require a minimum of four legs (with one leg in motion while the other three provide support), although it's common for them to have six legs [16][34].

Quadrupeds are renowned for their agility, while hexapods and myriapods are known for their stability. In contrast, limbless robots excel at maneuvering within confined spaces. However, as robots become more complex and feature a higher number of degrees of freedom (DoF), there arise coordination challenges in their motion. If these challenges are not effectively addressed, they can potentially render the robots impractical or non-functional [35]. The study presented in the paper by Chong et al. introduces a general framework for designing gaits in multilegged robots, including those with articulated backbones and even limbless sidewinding robots [35]. This framework combines two approaches to create self-deformation patterns, referred to as "gaits," which are essential for efficient locomotion across various robot configurations. The first approach draws inspiration from dimensionality reduction and biological gait classification schemes to produce cyclic patterns of body deformation and foot movement. The second approach extends geometric mechanics to frictional environments, optimizing body-leg coordination in terradynamic scenarios.

Importantly, the framework can be applied to robots with different numbers of limbs, including those with 4, 6, 16 limbs (Figure 2.2), or even those without limbs. The framework extends the Hildebrand gait formulation, initially used for symmetric quadrupedal gaits, and combines it with modern geometric mechanics tools to explore optimal leg-body coordination. It demonstrates that the symmetry observed in Hildebrand quadrupedal gaits is applicable to other locomoting systems. This framework is both straightforward for physical interpretation of gait parameters and versatile, covering a wide range of robot shapes and locomotion patterns [35].

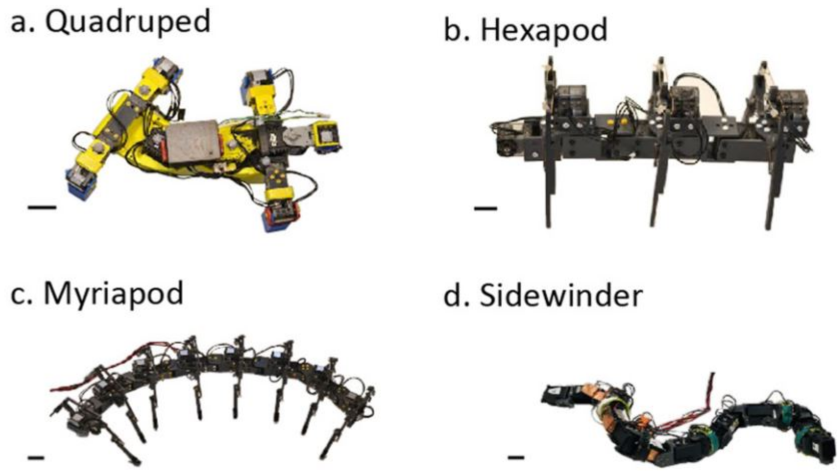

Figure 2.2: Legged and limbless robotic models studied in the paper. Used with permission of ref. [35]; permission conveyed through CCC, Inc.

In summary, robots are designed in diverse forms with unique advantages and challenges, enabling them to serve critical roles in various industries. Biomimetic locomotion in multi-legged robots, as described above, presents promising advancements in robotics, from soft appendages to magnetic actuation and gait planning [30][31][16][32]. These innovations offer potential solutions to overcome challenges in robotics and enhance adaptability in different environments.

2.2 The Structure and Function of Cilia

Cilia and flagella are both small-scale hair-like structures found in different types of cells in living organisms that serve different purposes for cell movement and function [36][37]. Cilia can transfer fluid within the cell or aid the cell in moving through fluid surroundings because of their distinctive back-and-forth, rhythmic beating motion [7]. The cilia that line the human respiratory tract help move mucus and trapped particles out of the lungs, helping the body protect itself from pathogens and debris [38][39]. Cilia in the brain, found on ependymal cells, serve vital roles in facilitating cerebrospinal fluid flow [40]. In some organisms, cilia help the movement of sperm cells [39]. In animal systems, densely packed ciliary arrays display a range of emerging phenomena, such as active filtration, resilience to noise, and the presence of metachronal waves [36].

Recent advances in microscopy and image analysis have enabled the integration of quantitative measurements of ciliary dynamics with a refined understanding of ciliary ultrastructure [36]. This progress has resulted in more accurate assessments and expla-

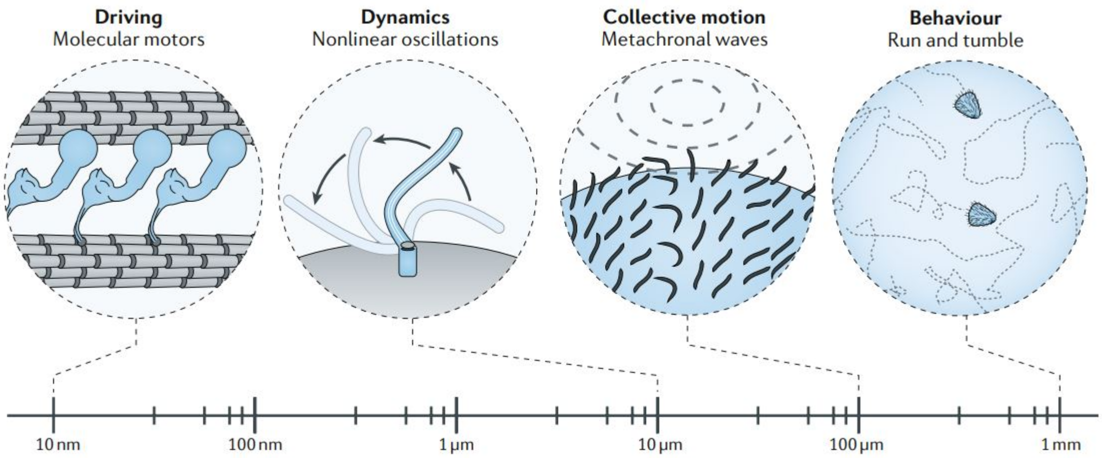

Figure 2.3: Cilliary motion across scales. Used with permission of ref. [36]; permission conveyed through CCC, Inc.

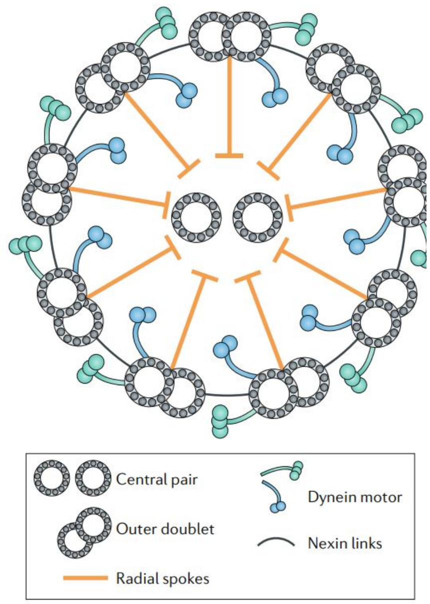

Figure 2.4: A cross-sectional view of a typical axoneme, which serves as the structural framework for a cilium, reveals the characteristic '9+2' arrangement of microtubule doublets. This arrangement consists of nine outer doublets encircling a central pair of microtubules, forming a distinctive pattern. Used with permission of ref. [36]; permission conveyed through CCC, Inc.

nations of the phase and periodicity of ciliary beating. As illustrated in Figure 2.3, the authors [36] systematically organize their exploration across different scales, revealing the transient synchronization of pairs of cilia and flagella through hydrodynamic or direct mechanical coupling.

Cilia consist of a central structure called the axoneme (Figure 2.4), which is a tube-shaped arrangement of microtubules [36]. In eukaryotic cilia and flagella, these microtubules are organized into nine doublets surrounding a central pair, known as a 9+2 arrangement as in Figure 2.4. This central pair of microtubules is crucial for defining the bending axis of the cilia. The outer microtubule doublets within the axoneme establish mechanical connections through nexin links, which surround and envelop a central pair of singlet microtubules [37]. The nexin link between microtubule doublets in 9 + 2 axonemal structures is critical for their ability to bend [37]. Additionally, each doublet has "radial spokes," which are protein complexes that extend toward the central pair of microtubules. These structural elements help maintain the integrity and stiffness of the axoneme. Dyneins are molecular motors found in the axonemal sheath, the structure that surrounds the microtubules. Dyneins are responsible for generating the force needed for cilia movement. They use the chemical energy from adenosine triphosphate (ATP) to create relative sliding motion among the nine microtubule doublets [36]. Cilia beating involves complex interactions between molecular motors (dyneins), the structural components of the axoneme, and proposed feedback mechanisms [36]. A feedback mechanism is a control system in which the result of a system is used as input to modify or adjust the behaviour of the system.

2.2.1 Bio-Inspired Robot Locomotion: Insights from Cilia Beating Patterns in Fluid Environments

To obtain a deeper understanding of how cilia beating patterns, as observed in nature, inspire novel improvements in robotics, our initial focus is directed toward their application within fluid environments. By understanding how cilia work in nature, engineers can develop robots that use similar mechanisms for efficient movement in fluids, which can be useful in underwater exploration or for designing efficient swimming robots.

In the context of ciliary motion, operating in a low Reynolds number regime within highly viscous fluids results in a significant dominance of viscous forces over inertial forces. As a consequence, the fluid strongly resists changes in velocity, causing any motion to damp out rapidly. In this overdamped scenario, cilia, the hair-like structures projecting from cells, don't experience significant inertial forces. Instead, their movements are primarily governed by viscous resistance. This unique environment allows cilia to effectively interact with one another through hydrodynamic interactions. The viscous fluid serves as a medium that transmits forces between neighboring cilia, facilitating the coordination of their beating patterns. The absence of substantial inertial effects and the prevalence of viscous forces result in collective motion where these structures coordinate and synchronize [7].

The sequential, wave-like motion resulting from metachronal coordination allows organisms to move more effectively against resistance, such as the viscosity of fluids, and is crucial for the locomotion of microorganisms, facilitating their ability to navigate and explore their environment. The main questions are how the properties of the metachronal wave, a wave-like pattern that has been found in cilia [14], are determined by the geometrical arrangement of the cilia, such as cilia spacing and beat direction, and how individual cilia interact with the flow field generated by their neighbors to synchronize their beats for the metachronal wave to emerge.

To address these questions, the study presented in [14] conducted large-scale computer simulations using a mesoscopic model of 2D cilia arrays in a 3D fluid medium. The research reveals that hydrodynamic interactions indeed explain the self-organization of metachronal waves and investigates various aspects, including beat patterns, stability, energy consumption, and transport properties. The results show that metachronal waves can significantly enhance propulsion velocity and efficiency compared to synchronized ciliary beating. This insight has implications for both biological experiments and the design of efficient microfluidic devices and artificial microswimmers.

The model represents cilia as semiflexible rods subject to active bending forces, with their beat pattern guided by the behaviour of paramecium, a unicellular organism that exhibits large arrays of cilia on its surface [14]. The dynamics of the surrounding fluid are described using a mesoscale hydrodynamic simulation technique that incorporates thermal fluctuations. In this model, cilia beat independently and are coupled via the fluid flow around them. The research aims to elucidate the formation and stability of metachronal waves in large cilia arrays and explores how these waves depend on factors like power-stroke direction and cilia spacing [14].

The study of Thomas Niedermayer et al. introduces a novel and simplified model for ciliary motion, with a specific focus on monocilia performing circular motions [7]. This model treats cilia as phase oscillators following circular trajectories with variable radii, allowing for analytical investigation of synchronization phenomena. The research shows that neighboring cilia couple through velocity fields generated in the surrounding fluid, resulting in hydrodynamic interactions that lead to collective effects [7].

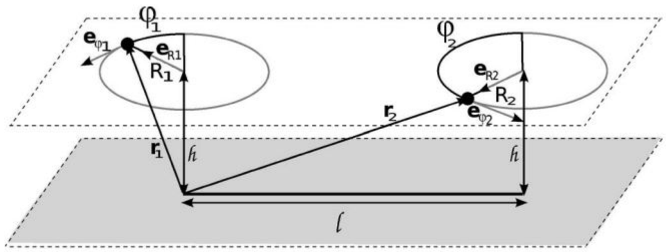

Figure 2.5: Stokeslet model for ciliary motion in hydrodynamic interactions:The cilium is approximated as a spherical bead with a radius a. The spherical bead follows a closed trajectory at a constant height h above the lipid membrane and r represents the position of the bead. Used with permission of ref. [7]; permission conveyed through CCC, Inc.

In this study, the researchers employed a "discrete cilia model" to calculate the velocity fields. In this model, they simplify the motion of the rotating monocilium by representing it as a spherical bead with a radius a following a closed trajectory at a height h above the lipid membrane. The "Stokeslet Model" (Figure 2.5), illustrates how the cilium is approximated as a spherical bead following a closed trajectory at a constant height above the lipid membrane.

In the exploration of collective effects within ciliary arrays, the examination of forces exerted by beating cilia on the surrounding fluid is crucial. These forces include the hydrodynamical drag force, which is the drag occurring between two beads in sequential motion, the internal driving force acting on the bead, and the restoring forces. The equation of motion for the bead is derived through the balance of these forces [7].

The researchers assume that the motion of cilia is overdamped, and therefore, inertial effects can be neglected. Consequently, the equations of motion for hydrodynamically coupled cilia resemble to the Kuramoto model. However, in contrast to Kuramoto's model, they assume that oscillators exclusively interact with their nearest neighbors, and the coupling function deviates from a sinusoidal form [7].

The study explores ciliary synchronization and motion revealing insights into rotating entities' behaviour within a Stokes fluid. Initially, the focus is on understanding interactions between two cilia, and the research demonstrates that synchronization can be analyzed in this context. The investigation then extends to considering a one-dimensional array of N cilia. By connecting several cilia in a linear chain, the researchers establish a phase oscillator model which allows for the emergence of metachronal waves. Simplifying the complexity of the system, this minimal model predicts the transitions to the synchronized and phase-locked state of two cilia and the formation of metachronal waves in ciliary chains under different boundary conditions [7].

The study conducted by Nariya Uchida and Ramin Golestanian focuses on the syn-

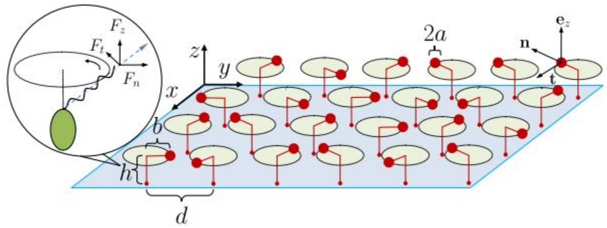

Figure 2.6: Schematic representation of the array of rotors. Used with permission of ref. [17]; permission conveyed by the American Physical Society.

chronization of an array of rotors on a substrate that are coupled by hydrodynamic interactions [17]. The research explores various dynamical behaviours of these rotors, which are modelled as effective rigid bodies driven by internal torques and exerting active forces on the surrounding fluid. The long-ranged nature of the hydrodynamic interaction between the rotors leads to a rich spectrum of behaviours, including phase ordering and self-proliferating spiral waves. The findings have implications for designing controllable microfluidic mixers utilizing the emergent behaviour of hydrodynamically coupled active components. The model consists of spherical beads moving along circular trajectories on a rectangular lattice. Each rotor is anchored on the substrate's surface (Figure 2.6).

Importantly, the circular constraint not only confines the rotor's movement but also causes it to drag the fluid tangentially along its circular path and pump the fluid radially due to internal degrees of freedom. The model is numerically solved using the Euler method with periodic boundary conditions, and the velocity field is computed at each time step using the Fourier transform [17]. In summary, the model proposed in [17] reveals a range of dynamic patterns, including global synchronization, fully disordered states, and the emergence of self-propagating spiral waves. These findings suggest the potential for designing arrays of active microfluidic components that can induce diverse dynamic behaviours in the surrounding fluid.

In the absence of hydrodynamic coupling, the coupling between filaments for terrestrial locomotion becomes more complex. This is because the robot has to rely more on its internal mechanical components for movement, making the dynamics of these components more complex. The overdamped hypothesis, originally applied in a fluid environment with strong damping effects, is no longer valid. Additionally, the governing equation for the system includes second-order derivatives.

2.3 Exploring Mechanical Coupling Strategies for Terrestrial Robot Locomotion

The majority of research in bio-inspired robotic locomotion using cilia-like protrusions has generally focused on understanding the operation of cilia-like appendages in the context of hydrodynamic coupling. This focus has primarily revolved around the study of coordination patterns among arrays of these filaments. Such research has been highly beneficial for the development of aquatic robots, designed to operate efficiently in water environments [41].

However, for terrestrial robots, there are different and distinct challenges in using this type of system for legged locomotion. Terrestrial environments present unique demands, necessitating a departure from the fluid-based strategy that works well in water. Specifically, the coupling among oscillating filaments, in the absence of the embedding fluid, is exerted via the base to which the oscillators are attached. The robot's motion is less dominated by external forces and more influenced by its internal mechanical properties. As a result, the phase dynamics are not dominated by damping, and the resulting governing equations are second order due to the non-negligible inertia. This poses new challenges with respect to existing literature in studying the coupled dynamics, and eventually predicting coordination patterns.

2.3.1 Studies in Coordination Patterns and Metachronal Waves for Terrestrial Locomotion

Simple artificial cilia can be actuated and set in motion using a time-varying magnetic field possibly inducing the metachronal waves seen in natural cilia [42]. The recent research in [15] introduces magnetically actuated, soft, artificial cilia carpets (Figure 2.7). These carpets are created by stretching and folding onto curved templates, allowing programmable magnetization patterns to be encoded into them. As a result, these artificial cilia carpets exhibit metachronal waves when exposed to dynamic magnetic fields. The study [15] offers an experimental platform for customized cilia carpets with a wide design space to facilitate fundamental studies of natural cilia, cilia-based active matter systems, and cilia-inspired soft robotic applications [15].

In the paper [18], an approach is presented to mimic metachronal motion observed in biological cilia through miniaturized metachronal arrays. The proposed method involves integrating a rod-shaped paramagnetic substructure beneath identical magnetic artificial cilia (MAC) and subjecting it to an external rotating magnetic field. The time-dependent

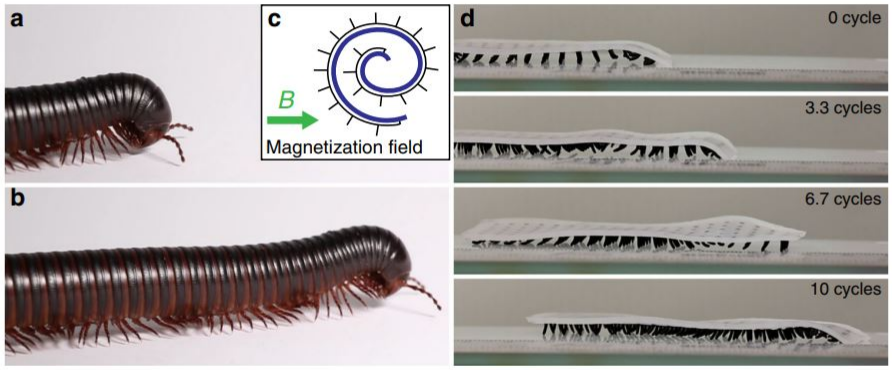

Figure 2.7: Millipede-inspired soft robot crawl using metachronal waves. a, b. A crawling giant African millipede. c. The magnetization template to magnetize the soft cilia carpet (20 × 5 cilia array) in the magnetizer. d. Experimental results of the crawling soft robot [15].

local magnetic field generated at the MAC location induces wave-like motions, replicating the metachronal behaviour of biological cilia. The motion of each magnetic artificial cilium is determined by the interplay between magnetic and elastic torques, influenced by the cilia's bending stiffness defined by its shape and size.

The study employs a combination of experimental and numerical methods, including finite element simulations using COMSOL, to validate and understand metachronal motion. Both experimental results and numerical simulations contribute to understanding the impact of inertia on flow generation at high Reynolds numbers (the ratio of fluid inertia to fluid drag force) in water and low Reynolds numbers in glycerol [18]. In their exploration, they found that altering the diameter or geometry of the substructure allowed for the adjustment of the wavelength of the metachronal motion. This flexibility was demonstrated in achieving metachronal motion in arrays with different numbers of magnetic artificial cilia (MAC), maintaining the same dimensions while varying the pitch between neighboring cilia and keeping a consistent beating frequency. The study's findings are illustrated through simulations, aligning parameters with those used in the experimental setup. Overall, the research demonstrates the effectiveness of their method in achieving miniaturized metachronal motion across various configurations, suggesting potential applications in fluid dynamics and biomimetic systems and contributing to the advancement of artificial cilia research.

In the study [15], the researchers introduce magnetically actuated, soft, artificial cilia carpets capable of exhibiting metachronal waves in dynamic magnetic fields. This stretchable magnetic cilia carpet consists of a large number (>200) of cilia hair structures, as shown in Figure 2.7. The study involves characterizing the motions of magnetic cilia under dynamic magnetic fields, developing a predictive model for metachronal motions resulting from different magnetization patterns, and investigating the transport and locomotion capabilities of the system. The model is based on the Cosserat rod theory, which is particularly suitable for simulating the elastic behaviour of slender, beam-like, soft magnetic structures like cilia.

In the study presented by Y. Collard et al., researchers investigated the behaviour of tiny soft ferromagnetic particles placed along a liquid interface in the presence of a vertical magnetic field [42]. They found that a balance between capillary attraction and magnetic repulsion led to self-organization of these particles into well-defined patterns. These patterns, when subjected to precessing magnetic fields, exhibited metachronal waves on their periphery, resembling the locomotion strategies observed in ciliates and some arthropods. The outermost layer of particles acted like an array of cilia or legs, creating sequential movements that resulted in controllable locomotion, even at low Reynolds numbers, using spatially uniform magnetic fields to generate the waves. The simple concept of the approach allowed for many possibilities, including complex self-assemblies and microsystems with engineered cilia for biomimetic propulsion and various applications.

In the study [8], a mechanical model is proposed for an array of elastic filaments exploring their response under various mechanical couplings. The study introduces a mechanical model featuring an array of elastic filaments anchored to a base, incorporating elastic couplings within the system. Each filament in this study is treated as a stiff polymer with an active internal force, aligning with the structural features of axonemal systems. The nonlinear rod kinematics incorporates curvature and a distributed system of internal shear forces. The study explores various feedback mechanisms for basal coupling and demonstrates how controlling actuation and coupling can generate different beating patterns, even when using the same material and geometric parameters.

2.3.2 Summary and Present Work

Various types of terrestrial robots, including wheeled, legged, bipedal humanoid, multilegged, and soft robots, offer diverse applications in industries such as manufacturing, agriculture, and search and rescue, each with specific advantages and challenges related to mobility, adaptability, and mechanical design. The field of biomimetic or biorobots involves designing robots inspired by biological organisms, utilizing structures and mechanisms found in nature. Recent studies showcase innovations such as a soft-legged quadruped robot with modular appendages for adaptability and a soft octopodal robot with magnetized locomotion for potential biomedical applications [30] [31]. The studies on terrestrial robots and biomimetic designs emphasize the vital need to understand how robot legs coordinate their movements for effective functioning.

The examination of metachronal coordination in cilia highlights its essential role in efficient movement, particularly in fluid environments. Computer simulations analyze metachronal wave properties, focusing on factors like cilia spacing and beat direction [14]. Hydrodynamic interactions are identified as key contributors to the self-organization of metachronal waves, improving propulsion efficiency compared to synchronized beating. A simplified model [7] for monocilia performing circular motions clarifies hydrodynamic interactions leading to collective effects. The study of forces exerted by beating cilia on the surrounding fluid is crucial, and a minimal model predicts transitions to synchronized states and metachronal waves in ciliary chains. In the study [17], the synchronization of rotors coupled by hydrodynamic interactions is explored, revealing a range of dynamic patterns with implications for designing controllable microfluidic mixers. Overall, these studies offer insights into the dynamics of biological and biomimetic systems, enhancing our understanding of metachronal coordination and its applications.

Research on bio-inspired robotic locomotion with cilia-like protrusions has mainly focused on understanding hydrodynamic coupling for aquatic robots, but applying such systems to terrestrial robots presents distinct challenges. Recent advancements in biomimetic research have led to significant strides in understanding mechanical coupling and metachronal coordination in artificial systems. For instance, the development of magnetically actuated artificial cilia carpets offers an experimental platform and demonstrates programmable metachronal waves, revealing coordination patterns similar to natural cilia. Similarly, exploring miniaturized metachronal arrays has provided insights into coordination mechanics and potential applications in fluid dynamics and biomimetic systems. Investigations into soft ferromagnetic particles have unveiled self-organization patterns resembling ciliate and arthropod locomotion, establishing a tangible link between mechanical coupling and coordinated movements. Furthermore, the mechanical model for elastic filament arrays enhances our comprehension of diverse beating patterns, illustrating the impact of controlled actuation and coupling on metachronal coordination. These findings deepen our understanding of the interplay between mechanical coupling and metachronal coordination.

This thesis initiates by modelling the system without hydrodynamic coupling, resulting in second-order dynamics. The model incorporates interconnected filaments, resembling biological cilia, connected by visco-elastic springs at their base. The primary goal is to model and simulate the system, exploring coordination patterns in arrays of coupled filaments across various parameter settings. The preliminary results obtained by this thesis will guide future work in predicting emergent coordination patterns and quantitatively addressing wave propagation associated with synchronization and metachronal coordination. This foundational work is directed towards designing mechanical systems for terrestrial locomotion, aiming to enhance robot capabilities for navigating diverse terrains.

Chapter 3

System's Model

The focus of this thesis project is modelling the dynamics of coupled filaments arranged as a planar lattice. In this chapter, we discuss the model, including its formulation and underlying principles. Our primary objective is to construct a lattice structure comprised of coupled filaments, which we conceptualize as upward oscillators interconnected by visco-elastic elements. Here we discuss the hypotheses that lead to the model of the system, and derive the governing equations using the Lagrangian approach.

3.1 Modelling Assumptions and Definitions

The system of coupled filaments is arranged in a two-dimensional grid or lattice. The filaments are connected via a solid substrate or base, to which they are attached in a lattice configuration, as illustrated in Figure 3.1. A lumped-parameter model is adopted, in which the mass of the base, or substrate, is lumped at the attachment points, and the filaments are modelled as rigid bodies with mass lumped at the tip. This configuration is illustrated in Figure 3.1. The visco-elastic properties of the base are lumped into springs and dampers connecting geometrically contiguous oscillators at the attachment sites. The

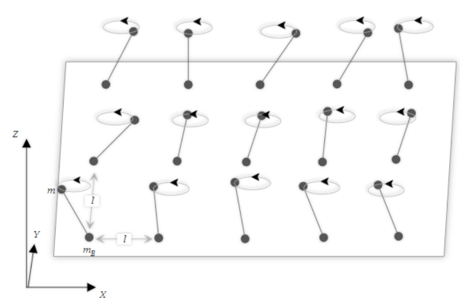

Figure 3.1: Rigid filaments on the lattice plane

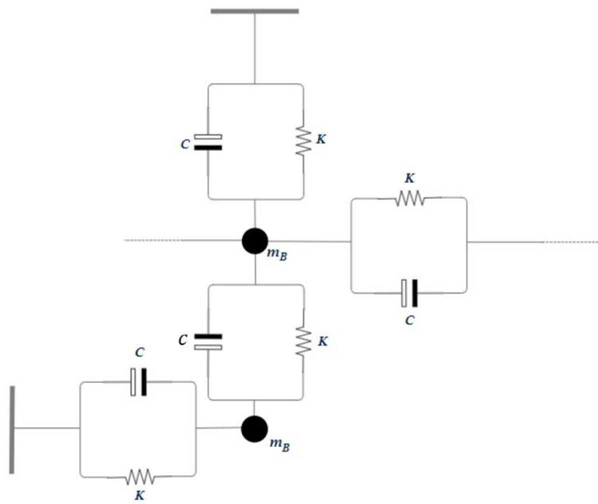

Figure 3.2: Lumped mass model with visco-elastic properties, where K is the stiffness coefficient, C is the viscous damping coefficient and m_B is the mass concentration at the base.

ones on the boundary are connected to the wall through grounded springs, which prevent rigid-body modes.

A schematic of the lumped-parameter model of the base is presented in Figure 3.2, restricted to a portion to highlight the connection between attachment sites of the oscillators.

3.1.1 Geometry and Lagrangian Coordinates

Within the lumped-parameter model of the system, each point in the lattice is a discrete unit. Sites on the lattice are identified by two discrete indices, i and j, where i ranges from 1 to n_x, and j ranges from 1 to n_y. These indices correspond to two-dimensional spatial coordinates (x, y) where x represents positions along the x-axis and y represents positions along the y-axis in the Cartesian coordinate system (see Figure 3.1). The parameters n_x and n_y define the number of points distributed along the respective axes.

The location of the basis of oscillator ij can be described in the Cartesian coordinates (x_{ij}, y_{ij}), or in the polar coordinates (R_{ij}, θ_{ij}), where R_{ij} is the radial coordinate, signifying the distance from the origin of a global reference frame to the lattice point defined by (i, j), and θ_{ij} represents the angle, indicating the angle formed between the positive x-axis and the line connecting the origin to the lattice point (i, j). As shown in Figure 3.4, the polar coordinates are described by the following equations:

$$
\begin{aligned}
R_{ij} &= \sqrt{x_{ij}^2 + y_{ij}^2} \\
\theta_{ij} &= \arctan\left(\frac{y_{ij}}{x_{ij}}\right)
\end{aligned}
\tag{3.1}
$$

The position vector of the base, as illustrated in Figure 3.3, can be described by the following equation:

$$
\begin{aligned}
r_B(t)_{ij} &= (x_{ij}(t), y_{ij}(t)), \\
&= (R_{ij}(t)\cos(\theta_{ij}(t)), R_{ij}(t)\sin(\theta_{ij}(t)))
\end{aligned}
\tag{3.2}
$$

where $i = 1, ..., n_x$ and $j = 1, ..., n_y$. The position of the oscillator's free extremity with respect to the base attachment site is described using spherical coordinates, specifically $(\rho_{ij}, \phi_{ij}, \varphi_{ij})$. In this coordinate system, ρ_{ij} represents the length of the oscillator, ϕ_{ij} corresponds to the co-latitude angle, and φ_{ij} is the longitude angle as illustrated in Figure 3.4.

The relative position of the tip of oscillator ij with respect to the attachment point on the substrate/base (or the lattice location ij) is expressed in the global frame of reference in terms of the set of spherical coordinates $\rho_{ij}, \phi_{ij}, \varphi_{ij}$ as follows:

$$
r_{BC}(t)_{ij} = \begin{pmatrix} x_{ij}(t) \\ y_{ij}(t) \\ z_{ij}(t) \end{pmatrix} = \begin{pmatrix} \rho_{ij}(t)\sin(\phi_{ij}(t))\cos(\varphi_{ij}(t)) \\ \rho_{ij}(t)\sin(\phi_{ij}(t))\sin(\varphi_{ij}(t)) \\ \rho_{ij}(t)\cos(\phi_{ij}(t)) \end{pmatrix}
\tag{3.3}
$$

Then the position vector for the free end can be defined as follows (see Figure 3.3):

$$
\begin{aligned}
r_{ij}(t) &= r_B(t)_{ij} + r_{BC}(t)_{ij} \\
&= \begin{pmatrix} R_{ij}(t)\cos(\theta_{ij}(t)) + \rho_{ij}(t)\sin(\phi_{ij}(t))\cos(\varphi_{ij}(t)) \\ R_{ij}(t)\sin(\theta_{ij}(t)) + \rho_{ij}(t)\sin(\phi_{ij}(t))\sin(\varphi_{ij}(t)) \\ \rho_{ij}(t)\cos(\phi_{ij}(t)) \end{pmatrix}
\end{aligned}
\tag{3.4}
$$

where $R_{ij}(t)$ and $\theta_{ij}(t)$ are associated with polar coordinates and $\rho_{ij}(t)$, $\phi_{ij}(t)$, and $\varphi_{ij}(t)$ are associated with spherical coordinates as in Figure 3.4.

Within this geometric representation, each oscillator has 5 degrees of freedom, in terms of two planar coordinates of the lumped mass at the base m_B and three spherical coordinates to describe the relative position of the lumped mass at the tip m. Therefore, we

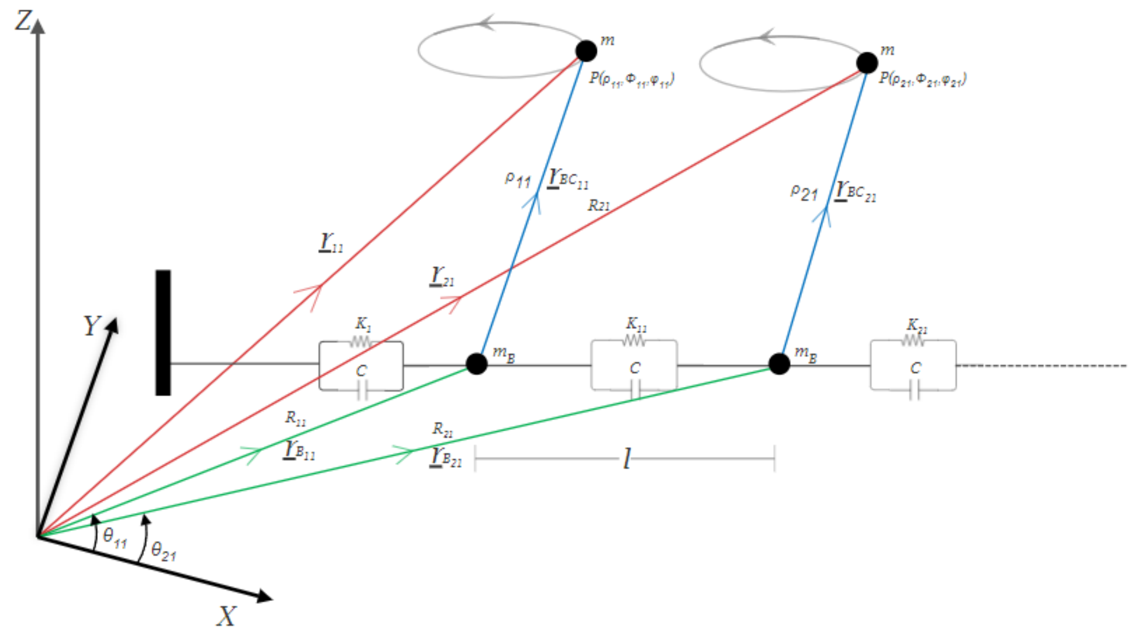

Figure 3.3: Parametric representation of two mass-loaded rotating oscillators with lumped viscous-elasticity.

adopt the following set of Lagrangian coordinates for each oscillator:

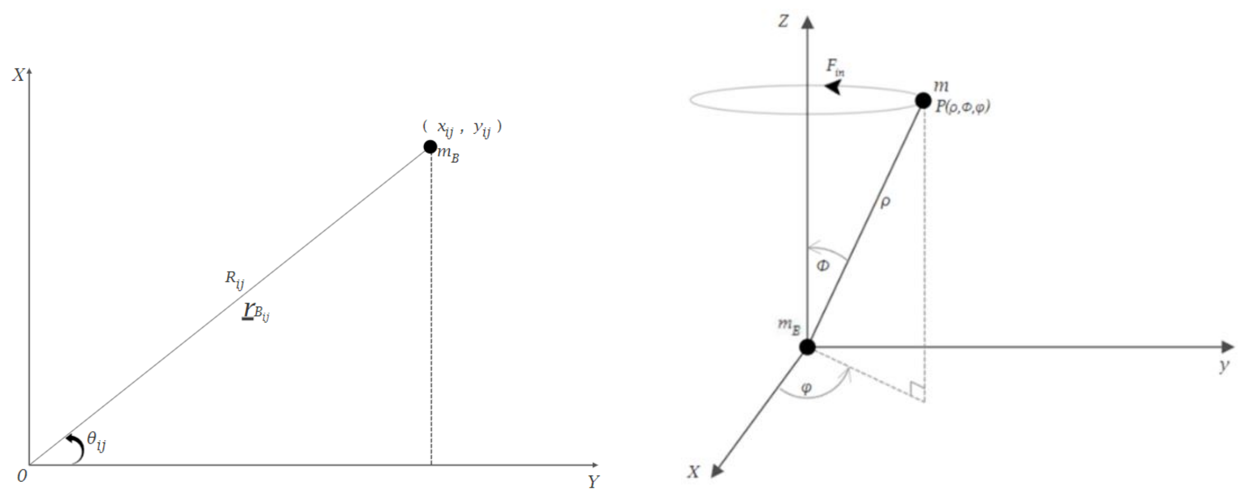

Figure 3.4: Polar coordinates $(R_{ij}(t),(\theta_{ij}(t))$ (Left) and the spherical coordinates $(\rho_{ij}(t),\phi_{ij}(t),\varphi_{ij}(t))$ defining the position of the free end (Right).

$$q_{ij} = (R_{ij},\theta_{ij},\rho_{ij},\phi_{ij},\varphi_{ij}) \tag{3.5}$$

3.2 Model Formulation

Euler-Lagrange's equations yield a set of second-order ordinary differential equations, enabling the derivation of governing equations for a system defined by a set of generalized coordinates. To establish the Lagrangian function $L = T - V$, we need to derive the kinetic energy T and the potential energy V.

3.2.1 Kinetic Energy

The kinetic energy T of the system is calculated based on the positions and velocities of the oscillators.

The total kinetic energy of the system is described by the following equation:

$$T_{ij} = \frac{1}{2} m \Big(\frac{dr_{ij}(t)}{dt} \Big) . \Big(\frac{dr_{ij}(t)}{dt} \Big) + \frac{1}{2} m_B \Big(\frac{dr_B(t)_{ij}}{dt} \Big) . \Big(\frac{dr_B(t)_{ij}}{dt} \Big) \tag{3.6}$$

where m is the mass concentration at the tip and m_B is the mass concentration at the base.

The expressions for the time derivatives $\frac{dr_B(t)_{ij}}{dt}$ and $\frac{dr_{ij}(t)}{dt}$ of the position vectors $r_B(t)_{ij}$ and $r_{ij}(t)$ defined in equation (3.4) and equation (3.2) are obtained in Mathematica using the symbolic manipulation features of the software. The following expressions are obtained, with details of the code given in Appendix A:

$$\frac{dr_{ij}(t)}{dt} = \begin{bmatrix} \cos(\theta_{ij}(t))\dot{R}_{ij}(t) - R_{ij}(t)\sin(\theta_{ij}(t))\dot{\theta}_{ij}(t) + \cos(\phi_{ij}(t))\sin(\varphi_{ij}(t))\dot{\rho}_{ij}(t) + \\ \cos(\phi_{ij}(t))\cos(\varphi_{ij}(t))\rho_{ij}(t)\dot{\phi}_{ij}(t) - \sin(\phi_{ij}(t))\sin(\varphi_{ij}(t))\rho_{ij}(t)\dot{\varphi}_{ij}(t) \\ \sin(\theta_{ij}(t))\dot{R}_{ij}(t) + \cos(\theta_{ij}(t))R_{ij}(t)\theta_{ij}(t) + \sin(\phi_{ij}(t))\sin(\varphi_{ij}(t))\dot{\rho}_{ij}(t) + \\ \cos(\phi_{ij}(t))\sin(\varphi_{ij}(t))\rho_{ij}(t)\dot{\phi}_{ij}(t) + \cos(\varphi_{ij}(t))\sin(\phi_{ij}(t))\rho_{ij}(t)\dot{\varphi}_{ij}(t) \\ \cos(\phi_{ij}(t))\dot{\rho}_{ij}(t) - \sin(\phi_{ij}(t))\rho_{ij}(t)\dot{\phi}_{ij}(t) \end{bmatrix} \tag{3.7}$$

and

$$\frac{dr_B(t)_{ij}}{dt} = \begin{bmatrix} \cos(\theta_{ij}(t))\dot{R}_{ij}(t) - R_{ij}(t)\sin(\theta_{ij}(t))\dot{\theta}_{ij}(t) \\ \sin(\theta_{ij}(t))\dot{R}_{ij}(t) + R_{ij}(t)\cos(\theta_{ij}(t))\dot{\theta}_{ij}(t) \\ 0 \end{bmatrix} \tag{3.8}$$

To calculate the total kinetic energy T of the system, we sum the contributions from all the oscillators in the lattice. Using Mathematica, from the expressions of the time derivatives above, we obtain

$$T = \sum_{i,j=1}^{n_x,n_y} T_{ij} \tag{3.9}$$

$$
\begin{aligned}
T =& \frac{1}{2} m_B \sum_{i,j=1}^{n_x,n_y} \Big(\big(\sin(\theta_{ij}(t)) \dot{R}_{ij}(t) + \cos(\theta_{ij}(t)) R_{ij}(t) \dot{\theta}_{ij}(t) \big)^2 \\
& + \big(\cos(\theta_{ij}(t)) \dot{R}_{ij}(t) - R_{ij}(t) \sin(\theta_{ij}(t)) \dot{\theta}_{ij}(t) \big)^2 \Big) \\
& + m \sum_{i,j=1}^{n_x,n_y} \Big(\big(\cos(\phi_{ij}(t)) \dot{\rho}_{ij}(t) - \sin(\phi_{ij}(t)) \rho_{ij}(t) \dot{\phi}_{ij}(t) \big)^2 \\
& + \big(\sin(\theta_{ij}(t)) \dot{R}_{ij}(t) + \cos(\theta_{ij}(t)) R_{ij}(t) \dot{\theta}_{ij}(t) \\
& + \sin(\phi_{ij}(t)) \sin(\varphi_{ij}(t)) \dot{\rho}_{ij}(t) + \cos(\phi_{ij}(t)) \sin(\varphi_{ij}(t)) \rho_{ij}(t) \dot{\phi}_{ij}(t) \\
& + \cos(\varphi_{ij}(t)) \sin(\phi_{ij}(t)) \rho_{ij}(t) \dot{\varphi}_{ij}(t) \big)^2 \\
& + \big(\cos(\theta_{ij}(t)) \dot{R}_{ij}(t) - R_{ij}(t) \sin(\theta_{ij}(t)) \dot{\theta}_{ij}(t) \\
& + \cos(\varphi_{ij}(t)) \sin(\phi_{ij}(t)) \dot{\rho}_{ij}(t) + \cos(\phi_{ij}(t)) \cos(\varphi_{ij}(t)) \rho_{ij}(t) \dot{\phi}_{ij}(t) \\
& - \sin(\phi_{ij}(t)) \sin(\varphi_{ij}(t)) \rho_{ij}(t) \dot{\varphi}_{ij}(t) \big)^2 \Big)
\end{aligned}
$$

3.2.2 Potential Energy

The total potential energy of the system is determined by the contribution of the linear storage elements (linear springs) and by the gravity acting on the masses lumping the inertial properties of the oscillators. Specifically, the linear storage elements are the springs lumping the elastic properties of the oscillator's base, which inter-connect the oscillators, and ground the boundary ones on the lattice. Additionally, stabilizing rotational springs acting on the co-latitude coordinates ϕ_{ij} are added, as well as stabilizing translational springs acting along the radial coordinates ρ_{ij}. The different contributions are discussed individually, and summed to obtain the total potential energy.

- **Coupling Potential Energy** (V_{ij})**:** This term represents the potential energy associated with the coupling between neighboring oscillators (see Figure 3.5) via the lumped elasticity of the basis, expressed in terms of translational linear springs:

$$
V_{ij} = \frac{1}{2} \sum_{h,k=1}^{n_x,n_y} K_{ijhk} \sigma_{ijhk} (||r_B(t)_{ij} - r_B(t)_{hk}|| - l)^2 \tag{3.10}
$$

  where K_{ijhk} describes the coupling strength between oscillator ij and oscillator hk. The parameter l denotes the initial distance between two attachment points, which is uniform across all oscillators. The term σ_{ijhk} (Eq. 3.11) is an indicator introduced to extend the summation globally rather than restricting it to contiguous sites, taking

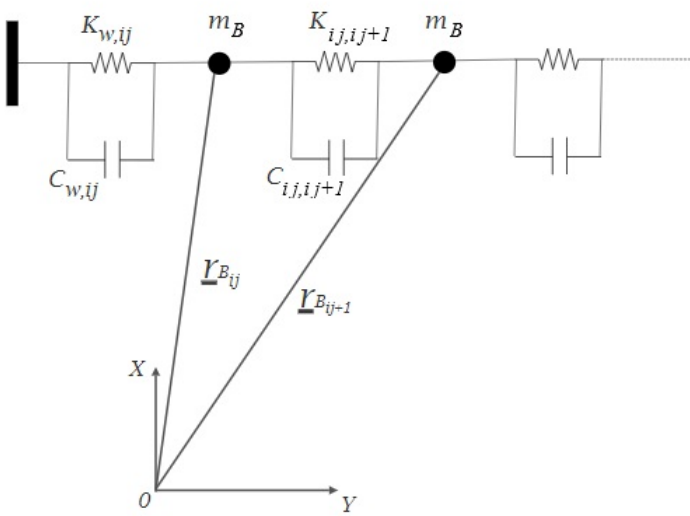

Figure 3.5: Lumped mass at the base coupled by visco-elastic properties.

the value of 1 if the oscillators ij and hk are connected and 0 otherwise:

$$\sigma_{ijhk} = \begin{cases} 1 & if \;\; hk \;\; connected \;\; to \;\; ij \\ 0 & Otherwise \end{cases} \tag{3.11}$$

From Mathematica, the expressions for the coupling potential energy between two neighboring oscillators are obtained as follows:

$$\begin{aligned} V_{ij} =& \frac{1}{2} K_{ij,ij+1} \sigma_{ijhk} [(-\cos(\theta_{ij}(0)) R_{ij}(0) + \cos(\theta_{ij}(t)) R_{ij}(t) \\ &+ \cos(\theta_{ij+1}(0)) R_{ij+1}(0) - R_{ij+1}(t) \cos(\theta_{ij+1}(t)))^2 \\ &+ (-R_{ij}(0) \sin(\theta_{ij}(0)) + R_{ij}(t) \sin(\theta_{ij}(t)) \\ &+ R_{ij+1}(0) \sin(\theta_{ij+1}(0)) - R_{ij+1}(t) \sin(\theta_{ij+1}(t)))^2] \end{aligned} \tag{3.12}$$

where $\theta_{ij}(0)$ and $R_{ij}(0)$ represent the initial polar angle and the initial radial distance of oscillator ij from the origin of the global reference frame (Eq. (3.2)).

- **Ground Springs Potential Energy** (V_w)**:** The elements situated at the boundary are connected to adjacent walls through elastic springs, to prevent rigid-body modes.

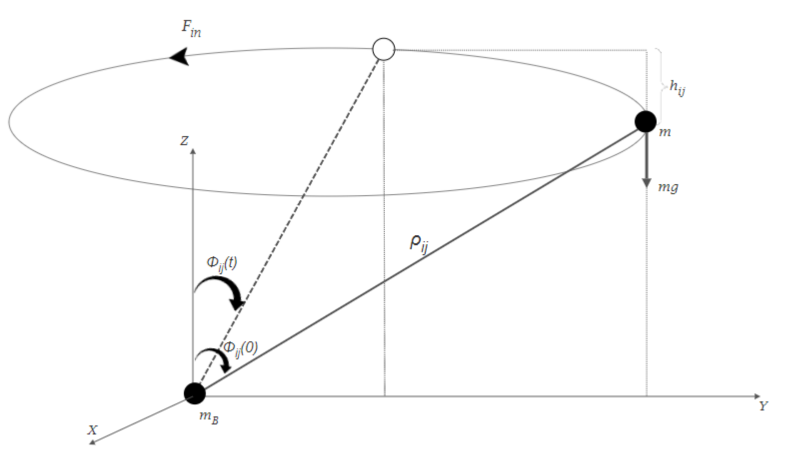

Figure 3.6: Spherical pendulum rotating around z-axis with height above the equilibrium position.

In the initial configuration $r_{ij}(0)$ in which the boundary oscillators are at rest, the potential energy of the ground springs is zero. Then, the total potential energy associated with the wall-connected springs is

$$V_w = \frac{1}{2} \sum_{i,j}^{n_x,n_y} K_w \lambda_{w,ij} \left\| r_B(t)_{ij} - r_B(0)_{ij} \right\|^2 \tag{3.13}$$

where K_w is the coupling strength with the wall, having the dimensions of stiffness, and $\lambda_{w,ij}$ is an indicator term which is equal to 1 if oscillator ij is connected to the wall and 0 otherwise, so that the summation can be extended globally. By simplifying the expression via the coordinates introduced in equation 3.2, we obtain the following expression:

$$V_w = \frac{1}{2} \sum_{i,j=1}^{n_x,n_y} K_w \lambda_{w,ij} [R_{ij}(0)^2 - 2\cos(\theta_{ij}(0) - \theta_{ij}(t)) R_{ij}(0) R_{ij}(t) + R_{ij}(t)^2] \tag{3.14}$$

- **Gravitational Potential Energy** (V_g)**:** The gravitational potential energy is due to the lumped mass at the tip of the filaments, which depends on the elevation h_{ij} above a reference point in the z-direction parallel to the direction of the acceleration g due to gravity, as sketched in Figure 3.6. By setting the reference on the plane xy of the base, the gravitational potential energy has the same expression as that of an inverted pendulum:

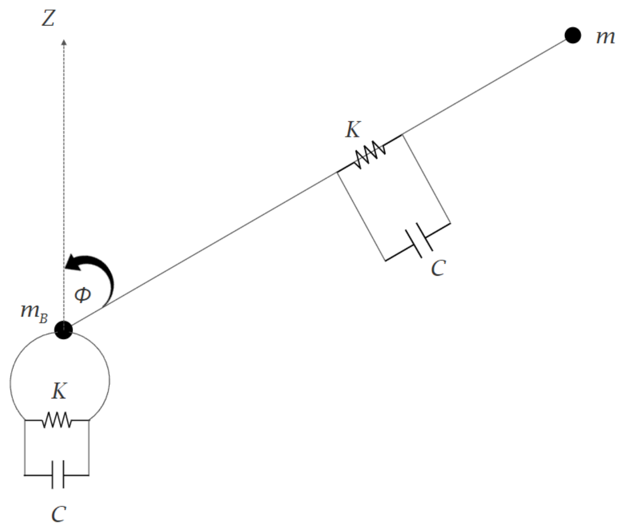

Figure 3.7: Spherical pendulum with restoring visco-elsticity along radius ρ and the co-latitude ϕ.

$$
\begin{aligned}
V_g &= -\sum_{i,j=1}^{n_x,n_y} mgh_{ij} \\
&= glm \sum_{i,j=1}^{n_x,n_y} \rho_{ij}(t)(1-\cos(\phi_{ij}(t)))
\end{aligned}
\tag{3.15}
$$

where h_{ij} is the elevation along the z coordinate, with respect to the reference at $\phi_{ij} = 0$.

- **Restoring Potential Energies from Lumped Elastic Properties of the Filaments:** The axial elastic restoring properties of each filament are lumped into a linear elastic spring acting along the radial coordinate ρ_{ij}, as shown in Figure, 3.7 resulting in the elastic restoring force:

$$
F_\rho = -K_\rho(\rho_{ij}(t) - \rho_{ij}(0)) \tag{3.16}
$$

where $\rho_{ij}(0)$ is the equilibrium length corresponding to zero restoring force, and taken as coincident with the initial condition. The corresponding potential energy

V_ρ along radial direction ρ is

$$V_\rho = \frac{1}{2}\sum_{i,j=1}^{n_x,n_y} K_\rho(\rho_{ij} - \rho_0)^2 \tag{3.17}$$

where K_ρ is the stiffness along the radial direction and $\rho_0 = \rho_{ij}(0)$ for all ij.

In order for the filaments to stand at the equilibrium around a co-latitude angle $\phi_{ij}(0)$ not on the base's plane, it is necessary to include a restoring torque with respect to this equilibrium (see Fig. 3.7). By assuming linearity, the restoring effect along the co-latitude coordinate is lumped to the rotational stiffness K_ϕ, resulting in the torque

$$T_\phi = -K_\phi(\phi_{ij}(t) - \phi_{ij}(0)) \tag{3.18}$$

The corresponding potential energy V_ϕ along the latitude angle ϕ is

$$V_\phi = \frac{1}{2}\sum_{i,j=1}^{n_x,n_y} K_\phi(\phi_{ij}(t) - \phi_{ij}(0))^2 \tag{3.19}$$

where K_ϕ is the stiffness along the latitude angle.

- **Total Potential Energy V:** The total potential energy of the system results from the summation of the distinct potential energy contributions outlined above.

$$V = V_{ij} + V_w + V_g + V_\rho + V_\phi. \tag{3.20}$$

3.2.3 Damping

The Rayleigh dissipation function is used to include linear damping effects into the Lagrangian formulation of the system [43]. When incorporated into the Lagrangian, it introduces dissipative Coulomb friction terms. Dissipation is expected to exist in the connecting material of the base, and within this model it is accounted for the coupling between oscillators as schematized in Figure 3.5. Moreover, in lumping the mass of each filament at the tip, elastic storage properties and dissipative properties should be accounted for along the axial coordinates ρ_{ij}. Finally, the interaction between each filament and the base is expected to include some dissipation, in the simplest form as friction between the two parts. Therefore, we include rotational dampers along the co-latitude ϕ_{ij} and the longitude φ_{ij} of each filament. These effects are individually discussed in the following.

- **Viscous Damping of Ground Attachment.** The Rayleigh's function term accounting for this effect is

$$R_w = \frac{1}{2} \sum_{i,j=1}^{n_x,n_y} C_w \lambda_{w,ij} ||\dot{r}_B(t)_{ij}||^2 \tag{3.21}$$

  Here C_w is the lumped viscous damping coefficient between the wall and the oscillator ij, $\lambda_{w,ij}$ is an indicator term which is equal to 1 if oscillator ij is connected to the wall and 0 otherwise, and $r_B(t)_{ij}$ is the position vector of the base as described in equation (3.2) and Figure 3.5.

  By manipulating the symbolic expressions with Mathematica, the expressions for the viscous damping due to ground attachment are obtained as follows:

$$\begin{aligned} R_w = \frac{1}{2} \sum_{i,j=1}^{n_x,n_y} C_w \lambda_{w,ij} [&(\sin(\theta_{ij}(t))\dot{R}_{ij}(t) + \cos(\theta_{ij}(t))R_{ij}(t)\dot{\theta}_{ij}(t))^2 \\ &+ (\cos(\theta_{ij}(t))\dot{R}_{ij}(t) - R_{ij}(t)\sin(\theta_{ij}(t))\dot{\theta}_{ij}(t))^2] \end{aligned} \tag{3.22}$$

- **Viscous Damping of Basal Coupling Between Two Contiguous Oscillators.**

$$R_{BC} = \frac{1}{2} \sum_{h,k=1}^{n_x,n_y} C_{ijhk} \sigma_{ijhk} ||\dot{r}_B(t)_{ij} - \dot{r}_B(t)_{hk}||^2 \tag{3.23}$$

  In the equation, C_{ijhk} represents the lumped viscous damping coefficient between the oscillators located at positions ij and hk, and σ_{ijhk} is the indicator introduced in equation (3.11). The position vectors of the base of these oscillators, denoted as $r_B(t)_{ij}$ and $r_B(t)_{hk}$, are defined as described in equation (3.2).

  By manipulating the symbolic expressions with Mathematica, the Rayleigh's function for the viscous damping due to coupling at the base of the oscillators is

$$\begin{aligned} R_{BC} = \frac{1}{2} \sum_{h,k=1}^{n_x,n_y} C_{ijhk} \sigma_{ijhk} [&(\sin(\theta_{ij}(t))\dot{R}_{ij}(t) - \sin(\theta_{ij+1}(t))\dot{R}_{ij+1}(t) \\ &+ \cos(\theta_{ij}(t))R_{ij}(t)\dot{\theta}_{ij}(t) - \cos(\theta_{ij+1}(t))R_{ij+1}(t)\dot{\theta}_{ij+1}(t))^2 \\ &+ (\cos(\theta_{ij}(t))\dot{R}_{ij}(t) - \cos(\theta_{ij+1}(t))\dot{R}_{ij+1}(t) \\ &- R_{ij}(t)\sin(\theta_{ij}(t))\dot{\theta}_{ij}(t) + R_{ij+1}(t)\sin(\theta_{ij+1}(t))\dot{\theta}_{ij+1}(t))^2] \end{aligned} \tag{3.24}$$

- **Damping Along ρ Direction**. The Rayleigh's function for the viscous damping along the radial coordinate of the filaments is

$$R_\rho = \frac{1}{2}\sum_{i,j=1}^{n_x,n_y} C_\rho(\dot{\rho_{ij}}(t))^2 \tag{3.25}$$

Here C_ρ is the viscous damping coefficient lumping the dissipation along the radial coordinate ρ_{ij}.

- **Damping Along ϕ Direction**. In formal analogy with the terms defined above, the Rayleigh's function for the viscous damping along the co-latitudinal coordinate of the filaments is

$$R_\phi = \frac{1}{2}\sum_{i,j=1}^{n_x,n_y} C_\phi(\dot{\phi_{ij}}(t))^2 \tag{3.26}$$

  Here C_ϕ is the rotational viscous damping lumping the dissipation along the co-latitude coordinate ϕ_{ij}. The linear damping approximation is described by the Rayleigh function R_ϕ quadratic in the rate $\dot{\phi}_{ij}$.

- **Damping Along φ Direction**. In formal analogy with the terms defined above, the Rayleigh's function for the rotational viscous damping along the longitudinal coordinate of the filaments is

$$R_\varphi = \frac{1}{2}\sum_{i,j=1}^{n_x,n_y} C_\varphi(\dot{\varphi_{ij}}(t))^2 \tag{3.27}$$

  Here C_φ is the viscous rotational damping coefficient lumping the linear dissipative effects along the longitude φ_{ij}. In simulation, all damping coefficients of the same type are the same for all filaments.

3.2.4 Euler-Lagrange Equations

The Euler-Lagrange equations are the equations of motion in the Lagrangian coordinates. These equations are derived from the Lagrangian of the system by minimizing the action functional, which is the integral of the Lagrangian over a time interval with prescribed generalized coordinates at the initial and final time [43]. The generalized coordinates, as defined in Section 3.1.1 and denoted by equation (3.5), are collected into a vector $q = (q_1, ..., q_n)$. The Euler-Lagrange equation for the k^{th} generalized coordinate is then expressed as follows:

$$\frac{d}{dt}\frac{\partial L}{\partial \dot{q}_k} - \frac{\partial L}{\partial q_k} + \frac{\partial R}{\partial \dot{q}_k} = Q_k^{\mathrm{NC}} \tag{3.28}$$

where $R = (R_w + R_{BC} + R_\rho + R_\phi + R_\varphi)$ and Q_k^{NC}, as defined in Section 3.2.3, is the generalized non-conservative external force along the generalized coordinate q_k [43].

In the derived model, the only non-zero generalized force is the internal driving force F_{in}, which is a torque along the longitudinal φ direction (see Figure 3.6)[7]. Therefore, the only non-zero generalized external force is $Q_k^{\mathrm{NC}} = F_{in}$ for $q_k = \varphi_k$, where k labels the set of filaments in the system.

3.2.5 Euler-Lagrange Equation with Mass Matrix

Since the kinetic energy (equation (3.9)) is quadratic in the generalized velocities $\dot{q}_k$, it is possible to introduce the mass matrix [43]

$$M(q) = \left[\frac{\partial^2 T}{\partial \dot{q}_i \partial \dot{q}_j}\right] \tag{3.29}$$

whose $(5n_x n_y + 1)/2$ independent components are in general nonlinear functions of the generalized coordinates.

The kinetic energy in terms of the mass matrix is given by [43][44]

$$T = \frac{1}{2}\dot{q} \cdot M(q)\dot{q} = \frac{1}{2}\sum_{i,j}^{n} M_{ij}(q)\dot{q}_i\dot{q}_j \tag{3.30}$$

By using the definition just introduced, we can rewrite Euler-Lagrange's equations by using the mass matrix:

$$\frac{\partial L}{\partial \dot{q}_k} = \sum_j M_{kj}\dot{q}_j \tag{3.31}$$

$$\frac{d}{dt}\frac{\partial L}{\partial \dot{q}_k} = \sum_j M_{kj}\ddot{q}_j + \sum_{i,j}\frac{\partial M_{kj}}{\partial q_i}\dot{q}_i\dot{q}_j \tag{3.32}$$

From the symmetry $M = \frac{1}{2}(M + M^T)$,

$$\frac{d}{dt}\frac{\partial L}{\partial \dot{q}_k} = \sum_j M_{kj}\ddot{q}_j + \frac{1}{2}\sum_{i,j}\frac{\partial M_{kj}}{\partial q_i} + \frac{\partial M_{ki}}{\partial q_j}\dot{q}_i\dot{q}_j \tag{3.33}$$

Since

$$-\frac{\partial L}{\partial q_k} = -\frac{\partial T}{\partial q_k} + \frac{\partial V}{\partial q_k} \tag{3.34}$$

from equations (3.30) and (3.33), we have the following form of Euler-Lagrangian equation:

$$\sum_j M_{kj}\ddot{q}_j + \frac{1}{2}\sum_{i,j}\left(\frac{\partial M_{kj}}{\partial q_i} + \frac{\partial M_{ki}}{\partial q_j} - \frac{\partial M_{ij}}{\partial q_k}\right)\dot{q}_i\dot{q}_j + \frac{\partial V}{\partial q_k} + \frac{\partial R}{\partial q_k} = Q_k^{\mathrm{NC}} \tag{3.35}$$

where R is the Rayleigh dissipation function, Q_{ijk} is the non-conservative generalized force and the operator $\Gamma_{ijk} = \frac{1}{2}\left(\frac{\partial M_{kj}}{\partial q_i} + \frac{\partial M_{ki}}{\partial q_j} - \frac{\partial M_{ij}}{\partial q_k}\right)$ is known as Christoffel symbols of the first kind, and it is related to the curvature of the configuration space referred to the coordinates q [45].

From the above equation, we define

$$C_{jk}(q,\dot{q}) = \sum_i \Gamma_{ijk}\dot{q}_i \tag{3.36}$$

$$K(q) = \frac{\partial V}{\partial q} \tag{3.37}$$

$$D(\dot{q}) = \frac{\partial R}{\partial \dot{q}} \tag{3.38}$$

By using the definitions just introduced, we can rewrite the Euler-Lagrange's equations in compact form:

$$M(q)\ddot{q} + C(q,\dot{q})\dot{q} + K(q) + D(q) = Q_k^{\mathrm{NC}} \tag{3.39}$$

where

$$\begin{aligned}
C(q,\dot{q}) &: \text{Coriolis matrix.}\\
K(q) = \frac{\partial V}{\partial q} &: \text{Vector of conservative forces.}\\
D(q) &: \text{Linear viscous damping forces.}\\
q &: \text{Vector of generalized coordinates.}\\
\dot{q} &: \text{Vector of generalized velocities.}\\
\ddot{q} &: \text{Vector of generalized accelerations.}
\end{aligned}$$

The governing equations illustrated here are obtained in explicit form in Mathematica, where they are also numerically solved. The long expressions in terms of generalized coordinates are given in Appendix A.

Chapter 4

Results and Discussion

4.1 Setup and Simulation Parameters

The dynamics of the system are described by equation (3.28). By using the Lagrangian formalism, the extended version of the governing equations, reported in Appendix A, was generated in Mathematica using its symbolic manipulation features (code in Appendix A), and numerically solved in the same environment using the built-in function "NDSolve", which solves nonlinear systems of ordinary differential equations. The primary goal of the simulation is to visualize, gain some insights, and understand of the type of coordinate patterns that evolve in an array of coupled oscillators. The ultimate goals are to predict the emergence of coordination patterns suitable for terrestrial locomotion, and apply them to robot design.

We set the initial conditions based on a set of key system parameters. These parameters are listed in Table 4.1 with their initial values. The rationale for the choice of the initial conditions is given below. The chosen set of parameters results in stable numerical solutions for the governing equations described in Chapter 3.

Parameter	Symbol	Initial Value
Length of each oscillator	ρ_0	0.04 m
Distance between two adjacent oscillators	l	0.08 m
Mass concentration at the tip	m	0.00104 kg
Mass concentration at the base	m_B	$m_B = Cm, C \in \mathbb{R}$
Co-latitude angle	ϕ_0	$\pi/3$
Damping due to ground spring	C_w	0.01 Nsm^{-1}
Damping due to spring connecting two adjacent oscillators	C_{BC}	0.01 Nsm^{-1}
Damping along ρ	C_ρ	0.1 Nsm^{-1}
Damping along ϕ	C_ϕ	1 Nsm^{-1}
Damping along φ	C_φ	0.001 Nsm^{-1}
Stiffness of the ground spring	K_w	20 Nm^{-1}
Stiffness of spring connecting two adjacent oscillators	K_{BC}	10 Nm^{-1}
Stiffness of the restoring term along ρ	K_ρ	20 Nm^{-1}
Stiffness of the restoring term along ϕ	K_ϕ	$K_\phi = 2mgl$
Acceleration due to gravity	g	9.81 ms^{-2}
Magnitude of the internal driving torque along φ	F_{in}	5 N
Time interval	t_f	10 s

Table 4.1: Model parameters and initial conditions for the simulations.

The filaments have a length of 4 cm, and the legs are cylindrical with a diameter of 0.8 cm, resulting in a ratio of 5:1 between the leg length and the diameter [15]. The legs were considered to be designed using silicon rubber compound EcoflexTM 00-30, with a density of 1.07 g/cm³ [15] [31] [30]. The legs of the robot are designed with a specific mass distribution, where the majority of the mass is concentrated at the tip m and the base m_B. This distribution follows a ratio of $m : m_B = C : 1$ where $C \in \mathbb{R}$.

The relationship between leg length and foot-to-foot spacing indicates that longer legs can enhance the robot's overall locomotion speed by enabling larger strides and increased velocity. The leg length to foot-to-foot spacing ratio typically ranges from 1 to 2 among most legged animals, reflecting their natural adaptation to balance speed and support in locomotion [31]. Based on this understanding, we set the leg length to foot-to-foot spacing ratio to 1:2. The initial distance among cilia attachment points at the base is denoted by l, corresponding to which the restoring forces in equation (3.10) are zero.

The initial co-latitude ϕ_0 is set to $\pi/3$, so that the oscillators are initially tilted with respect to the normal direction z with respect to the base, as illustrated in Figure 4.1. The stiffness and damping coefficients were chosen to achieve the desired coordinate patterns.

The variable F_{in} represents the magnitude of the internal driving torque along the longitude φ (see Figure 4.1). This driving torque is a lumped-parameter representation of the system of distributed internal action in axonemes and stiff flexible filaments, driving their beating dynamics. In the model used here, the beating dynamics is simply a rotation around the z axis, due to the rigid model for the filaments [7].

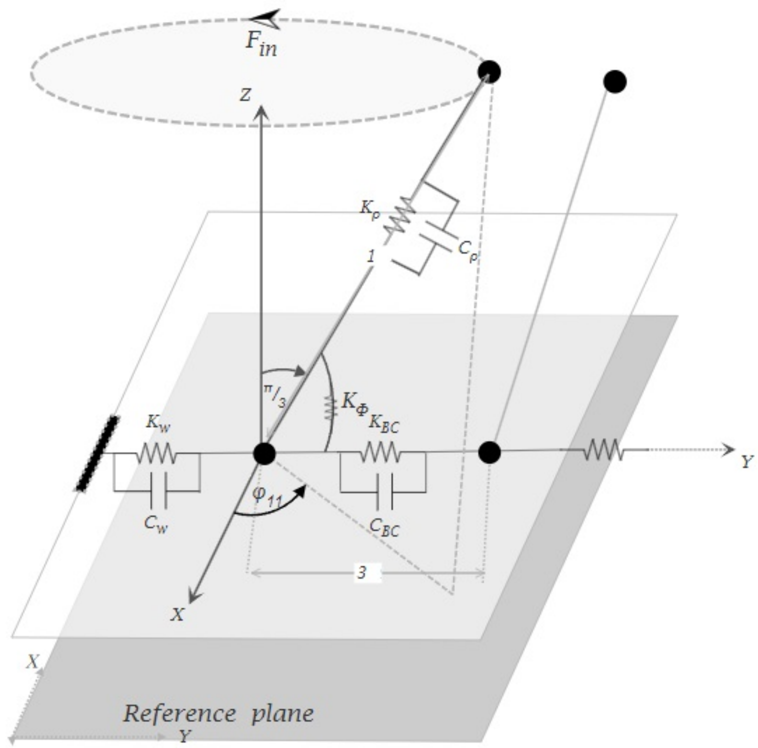

Figure 4.1: The initial configuration of robotic legs with parameters as listed in the Table 4.1

The initial conditions and system parameters for all the oscillators are the same as described in Table 4.1. In simulation, we analyze two sets of results. In the first set, a fixed phase difference of $\pi/4$ is initially set between adjacent oscillators, which corresponds to a metachronal configuration. The second set involves randomly assigned longitude values φ_0 drawn from the interval $[0, 2\pi]$. With the first set of initial conditions we want to check in simulation if the metachronal configuration is sustained. With the second set of initial conditions, we want to check if a metachronal configuration, or some other synchronized solution, emerges. For the purpose of locomotion, the variable φ is the relevant one; see Figure 4.1 [7]. These initial conditions, along with zero initial velocities, complete the setup for the subsequent numerical simulation.

The numerical solution is carried out using the **NDSolve** function in Mathematica, which is an adaptive multi-step nonlinear solver for systems of ordinary differential equations.

4.2 Parametric Analysis in Modelling and Simulation

A "metachronal wave" is a specific pattern of motion observed in an array of oscillators, particularly in the context of biological cilia [14]. In this pattern, adjacent oscillators within the array maintain a constant phase difference, leading to a distinctive wave-like motion. In dynamical systems terminology, this phase-locked state is similar to a travelling wave [7].

When studying metachronal waves, observing the evolution of longitude angle φ over time can provide insights into the coordination and phase relationships among the oscillators, which contribute to the wave-like motion along the oscillators. For the phase angle φ of oscillator ij, as expressed in equation (3.3) and illustrated in Figure 3.4, we will follow the definitions provided in [7].

Following [7], we introduce some definitions of quantities relevant for the simulations presented below.

1. **Definition: Synchronized State**
   In this context, the synchronized state for oscillator ij, where $i = 1, ..., n_x$ and $j = 1, \ldots, n_y$, is characterized by the condition where all oscillators within the array evolve with zero phase difference in terms of the longitude angle. Formally, this condition is expressed as

$$\varphi_{ij}(t) = \varphi_{ik}(t) \quad \text{for all} \quad k = 1, 2, \ldots, n_y \tag{4.1}$$

2. **Definition: Phase-Locked State**
   The phase-locked state refers to a condition in which the phases of the oscillators within the array become aligned. In a phase-locked state, all oscillators within an array exhibit identical phase with identical angular velocities, in terms of the longitude angles.

$$\dot{\varphi}_{ij}(t) = \dot{\varphi}_{ik}(t) \quad \text{for all } i = 1, \ldots, n_x \text{ and } j, k = 1, \ldots, n_y \tag{4.2}$$

   Here, $\dot{\varphi}_{ij}(t)$ represents the velocity of the longitude angle of oscillator ij.

3. **Definition: Metachronal Wave**

   Metachronal coordination in an array of oscillators refers to the state in which a constant phase difference among contiguous oscillators exists. This coordination manifests as a wave-like pattern propagating through the array:

$$\varphi_{ij+1}(t) = \varphi_{ij}(t) + \psi \quad \text{for all } i = 1, \ldots, n_x \text{ and } j = 1, \ldots, n_y - 1 \tag{4.3}$$

In equation (4.3), $\varphi_{ij}(t)$ represents the longitude angle of oscillator ij, $\varphi_{ij+1}(t)$ represents the longitude angle of the subsequent oscillator $ij+1$, and ψ represents the constant phase difference between oscillator ij and $ij+1$, which is the same for all ij. For metachronal waves, $\dot{\varphi}_{ij} \neq 0$, indicating non-zero angular velocities. This condition emphasizes the dynamic nature of the metachronal coordination.

4.2.1 Initial Metachronal Configuration

We consider a one-dimensional array of oscillators of dimension 1×8. We assume that all oscillators maintain a constant length denoted as ρ_0. With reference to the parameters detailed in Table 4.1, we consider the evolution in the longitude angle, φ, when the initial condition is a metachronal state with constant phase difference $\pi/4$ between pairs of contiguous oscillators.

Results are calculated for different combinations of some of the system's parameters, that may affect the dynamics.

- **Case 1**: Ratio between mass concentration at the base, m_B, and lumped mass of the oscillator, m, is 1. $\frac{m_B}{m} = 1$.

  Figure 4.2 depicts the variations in the longitude angle φ and the phase difference between two adjacent oscillators. In Figure 4.2c, the initial phase difference between oscillators shows some overshoot in their trajectories in the first few seconds. The initial phase differences between oscillators 1 and 2, 2 and 3, and 3 and 4 increase beyond 45° within the first few seconds, with their respective maximum points exceeding 45, 50, and 60 degrees. The peak of the initial overshoot in phase difference between oscillators 4 and 5, 5 and 6, 6 and 7, and 7 and 8 decreased. All trajectories rapidly decay after reaching their maximum values, settling at zero after around 2 seconds.

- **Case 2**: Ratio between mass concentration at the base, m_B, and lumped mass of the oscillator, m, is 5. $\frac{m_B}{m} = 5$.

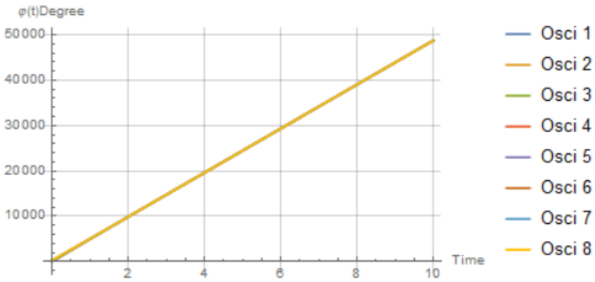

(a) $\varphi_{ij}(t)$ for the final time $t_f = 10s$

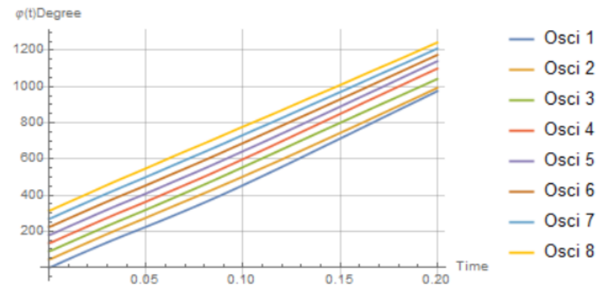

(b) $\varphi_{ij}(t)$ for the final time $t_f = 0.2s$

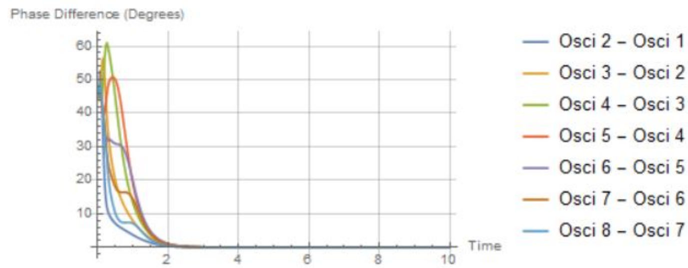

(c) $|\varphi_{ij+1}(t) - \varphi_{ij}(t)|$

Figure 4.2: Evolution of the longitude angle (a,b) and phase difference between two contiguous oscillators (c) in the case where $m_B = m$. The parameter configuration is provided in Table 4.1

Figure 4.3 illustrates the evolution of the longitude angle φ and its phase difference between adjacent oscillators, when the relation between lumped masses at the base and at the tip is $m_B = 5m$. In comparison to the previous case, similar behaviour can be observed in Figure 4.3c, the phase differences between adjacent oscillators. However, the settling time is slightly higher than in the previous case. The initial phase differences between oscillators 1 and 2, and 2 and 3, rise slightly above 45 degrees in the first few seconds, with the curve of oscillators 2 and 3 lying above the curve of oscillators 1 and 2. The phase differences between oscillators 3 and 4, 4 and 5, and 5 and 6 exhibit a concave-up curve after reaching their maximum values. The trajectory of oscillators 4 and 5 lies above the trajectory of oscillators 3 and 4, while the trajectory of oscillators 5 and 6 lies below that of oscillators 3 and 4, with each having a different rate of change in the curves. The phase differences between the oscillators 6 and 7, and 7 and 8, show a concave-down curve as they decrease, with the trajectory of oscillators 7 and 8 exhibiting a deeper curve than the previous trajectory. Overall, the settling time for each curve is above 10 seconds, indicating the sensitivity of the model when the mass concentration at the base is higher than that at the tip.

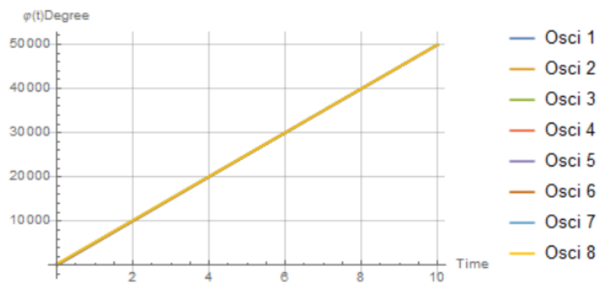

(a) $\varphi_{ij}(t)$ for the final time $t_f = 10s$

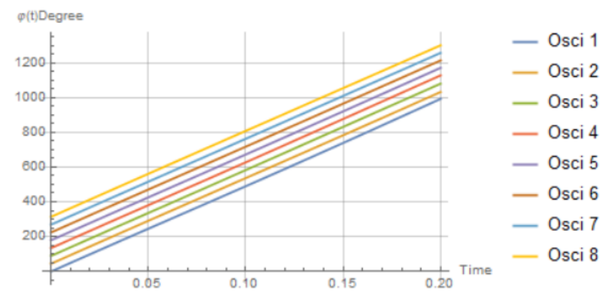

(b) $\varphi_{ij}(t)$ for the final time $t_f = 0.2s$

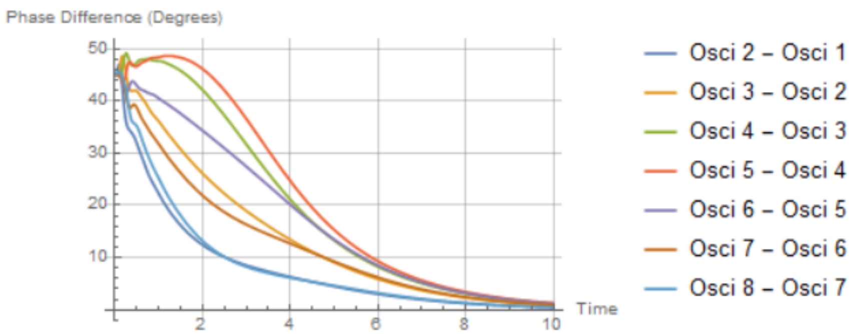

(c) $|\varphi_{ij+1}(t) - \varphi_{ij}(t)|$

Figure 4.3: Evolution of the longitude angle (a,b) and phase difference between two contiguous oscillators (c) in the case where $m_B = 5m$. The parameter configuration is provided in Table 4.1

- **Case 3**: Ratio between mass concentration at the base, m_B, and lumped mass of the oscillator, m, is $\frac{1}{5}$. $\frac{m_B}{m} = \frac{1}{5}$.

  Figure 4.4 depicts the evolution of the longitude angle φ and its difference between two adjacent oscillators in the array when the base-to-tip mass ratio is $m_B = \frac{1}{5}m$. Figure 4.4c exhibits a similar behaviour to that seen in Figure 4.2c when the mass ratio was 1. However, in this case, the time to reach the synchronized steady-state is shorter than that of case 1, indicating that when the mass concentration at the tip is higher than that at the base, the trajectories reach a stabilized state more quickly.

  In summary, when the initial condition is in a metachronal state with phase difference $\pi/4$ among contiguous oscillators, a consistent behaviour is observed across the three different cases simulated, where the initial metachronal state undergoes a transition to a synchronized state and there is zero phase difference between contiguous oscillators at steady state. According to the definitions in equations (4.1) and (4.2), this means that, eventually, all oscillators synchronize.

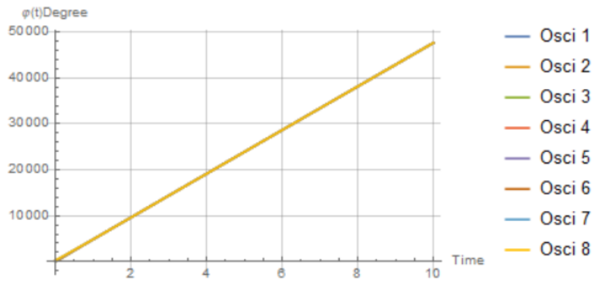

(a) $\varphi_{ij}(t)$ for the final time $t_f = 10s$

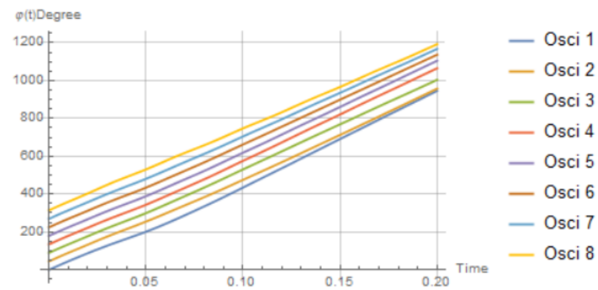

(b) $\varphi_{ij}(t)$ for the final time $t_f = 0.2s$

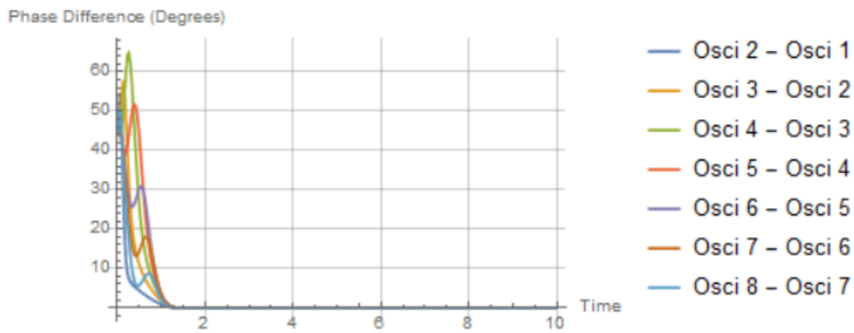

(c) $|\varphi_{ij+1}(t) - \varphi_{ij}(t)|$

Figure 4.4: Evolution of the longitude angle (a,b) and phase difference between two contiguous oscillators (c) in the case where $m_B = \frac{1}{5}m$. The parameter configuration is provided in Table 4.1

4.2.2 Initial Random Distribution of Oscillators' Longitudes

Initial longitude angle φ is randomly assigned from the interval $[0, 2\pi]$. The randomly assigned values for oscillators 1 to 8 are $210°, 24°, 113°, 288°, 127°, 252°, 46°$ and $154°$, respectively. The other parameters are selected as listed in Table 4.1.

- **Case 1:** Ratio between mass concentration at the base, m_B, and lumped mass of the oscillator, m, is 1. $\frac{m_B}{m} = 1$.

  The evolution of the longitude angle φ and the phase difference between contiguous oscillators is illustrated in Figure 4.5 when the base-to-tip mass ratio is $m_B = m$.

  Due to the random distribution of initial longitudes, the initial phase difference is heterogeneous among pairs of contiguous oscillators. As shown in Figure 4.5c, the initial phase differences between adjacent oscillators are $186°, 89°$,$175°$,$161°$,$125°$,$206°$ and $108°$, respectively. In Figure 4.5c, the phase differences between oscillators 1 and 2, 2 and 3, and 7 and 8 converge to zero degrees, while the phase differences between the rest of the pairs oscillators converge to $360°$. However, over time, the

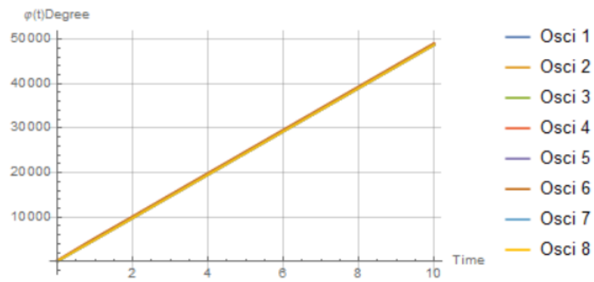

(a) $\varphi_{ij}(t)$ for the final time $t_f = 10s$

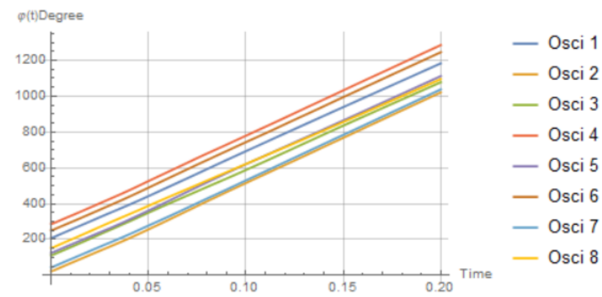

(b) $\varphi_{ij}(t)$ for the final time $t_f = 0.2s$

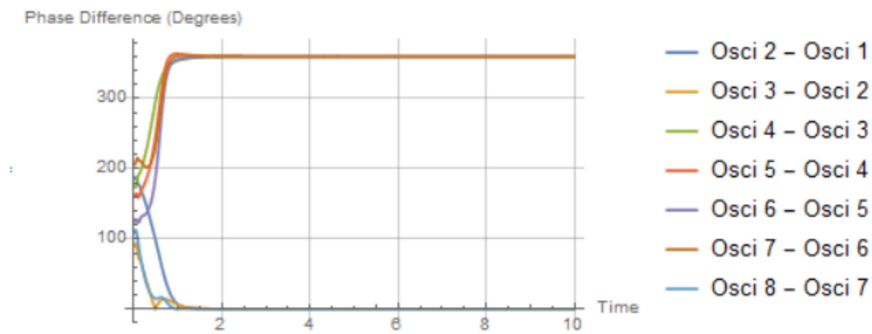

(c) $|\varphi_{ij+1}(t) - \varphi_{ij}(t)|$

Figure 4.5: Evolution of the longitude angle (a,b) and phase difference between two contiguous oscillators (c) in the case where $m_B = m$ with randomly distributed initial longitude angles, φ. The parameter configuration is provided in Table 4.1

phase differences converge to the same value (mod 2π), and the system reaches a synchronized state as with the metachronal initial condition simulated above, as depicted in Figure 4.5c.

- **Case 2:** Ratio between mass concentration at the base, m_B, and lumped mass of the oscillator, m, is 5. $\frac{m_B}{m} = 5$.

The evolution of the longitude angle φ and the phase difference between contiguous oscillators is depicted in Figure 4.6 when the base-to-tip mass ratio is $m_B = 5m$. In this scenario as well, the phase difference among contiguous oscillators converge to zero (mod 2π) and the oscillators reach a synchronized state. Compared to a similar case in the metachronal configuration described in Figure 4.3c, Figure 4.6c also shows an increased settling time, which is around 6 seconds.

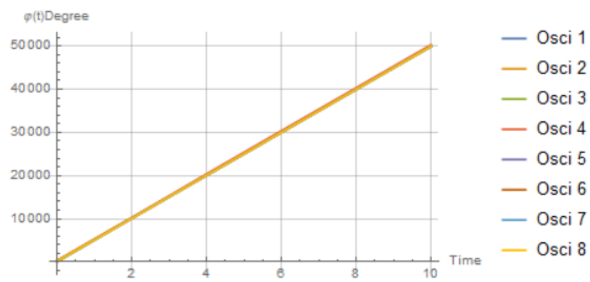

(a) $\varphi_{ij}(t)$ for the final time $t_f = 10s$

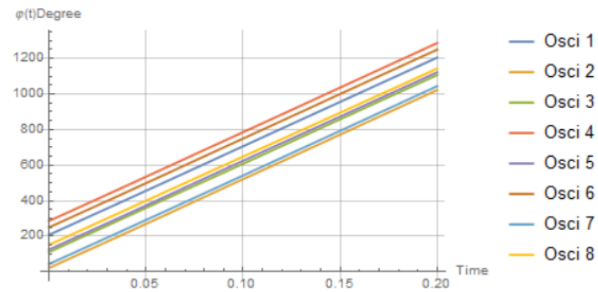

(b) $\varphi_{ij}(t)$ for the final time $t_f = 0.2s$

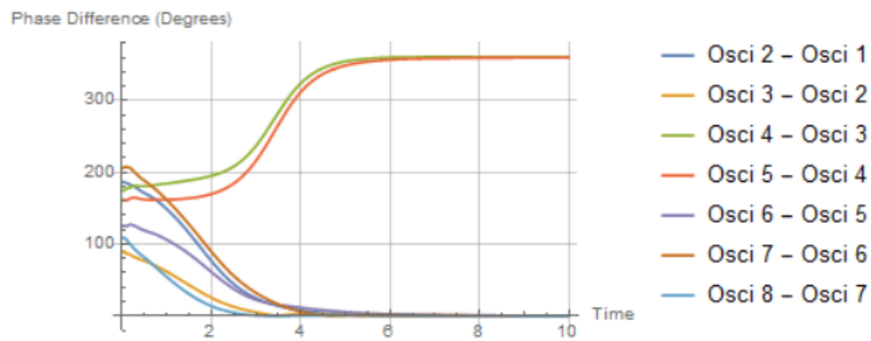

(c) $|\varphi_{ij+1}(t) - \varphi_{ij}(t)|$

Figure 4.6: Evolution of the longitude angle (a,b) and phase difference between two contiguous oscillators (c) in the case where $m_B = 5m$ with randomly distributed initial longitude angles, φ. The parameter configuration is provided in Table 4.1

- **Case 3:** Ratio between mass concentration at the base, m_B, and lumped mass of the oscillator, m, is $\frac{1}{5}$. $\frac{m_B}{m} = \frac{1}{5}$.

  The evolution of the longitude angle φ and the phase difference between contiguous oscillators is depicted in Figure 4.7 with the base-to-tip mass ratio being $m_B = \frac{1}{5}m$. As in the cases simulated before, the steady state of the system is a synchronized state with zero phase difference among pairs of contiguous oscillators.

  Confirming the patterns observed in previous simulation cases, the transient varies with the mass ratio, but the steady state seems to consistently converge to synchronicity.

In summary, when the initial longitudes are randomly assigned, the emergence of metachronal coordination is not observed in simulation for the cases considered here. A systematic analysis of the system's dynamics will be necessary for understanding how to predict such occurrence, which is relevant for terrestrial robot locomotion.

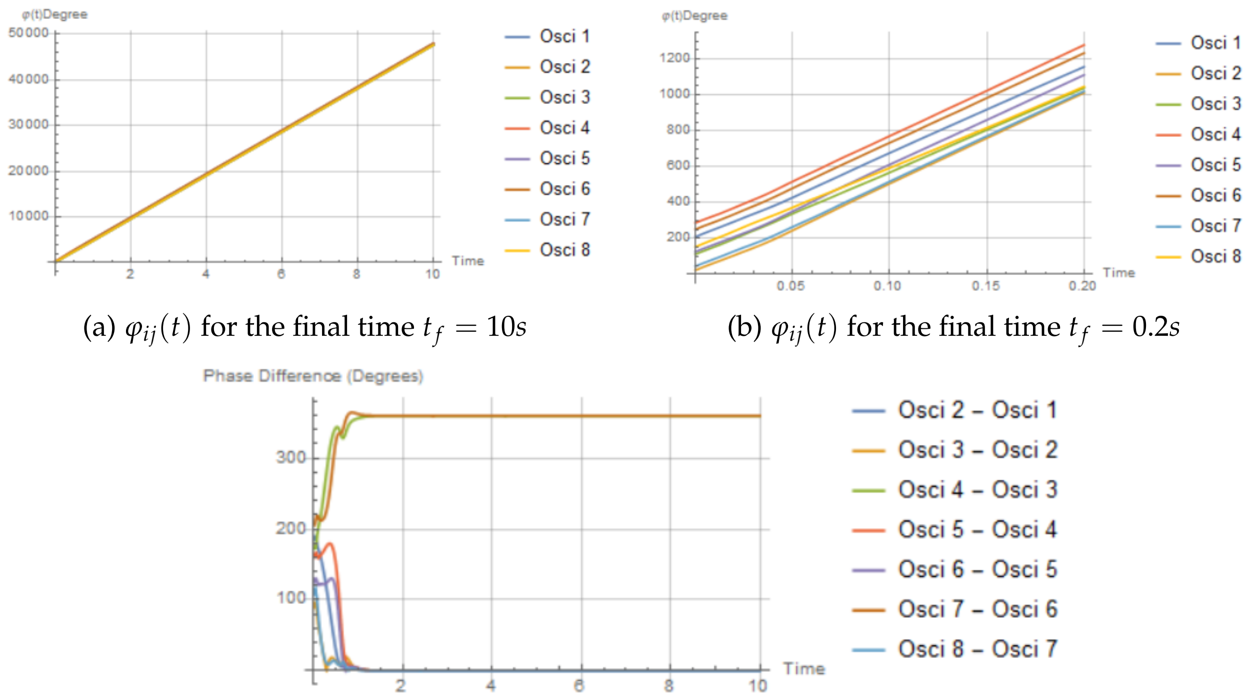

(a) $\varphi_{ij}(t)$ for the final time $t_f = 10s$

(b) $\varphi_{ij}(t)$ for the final time $t_f = 0.2s$

(c) $|\varphi_{ij+1}(t) - \varphi_{ij}(t)|$

Figure 4.7: Evolution of the longitude angle (a,b) and phase difference between two contiguous oscillators (c) in the case where $m_B = \frac{1}{5}m$ with randomly distributed initial longitude angles, φ. The parameter configuration is provided in Table 4.1

4.3 Simulation of Two-Dimensional Lattice Configurations

In this section, we present simulation results for a set of coupled oscillators arranged on a two-dimensional lattice configuration in terms of base attachment sites. The radius ρ evolves and it is not constant as in the simulations previously presented, and randomly distributed longitude angles within the interval $[0, 2\pi]$ are assigned on a 4×4 lattice. The 2D lattice configuration is depicted in Figure 4.8.

Figure 4.9a illustrates the evolution of the longitude angle φ and its derivative corresponding to the parameters outlined in Table 4.1. As shown in Figure 4.9b, the rate of change of the variation of longitude angles, φ, of each oscillator fluctuates initially, showing some distinct and different patterns, before settling at nearly a constant value.

Figure 4.10a depicts the evolution of the co-latitude angle, which is the same for all the oscillators initially. Over time, these angles converge to different distinct values.

Figure 4.10b illustrates the variation of the oscillators' length, ρ. Initially, all the oscillators have the same length, ρ_0, but over time, they converge to three different values.

Figure 4.11 illustrates the evolution of polar coordinates (R, θ) of the base sites attach-

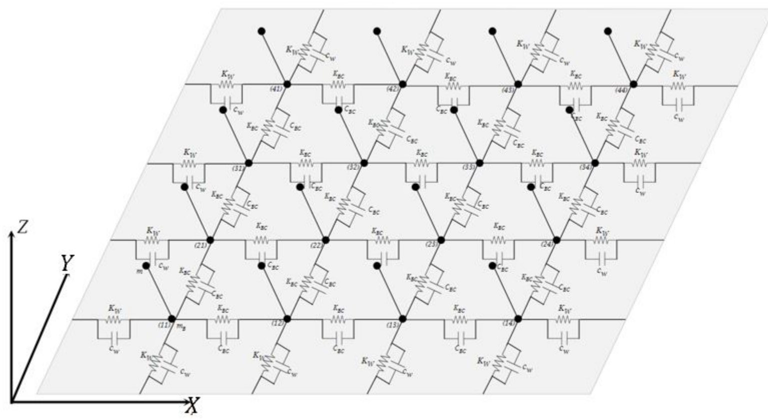

Figure 4.8: The oscillators in a 4×4 grid. $m_B = m$ for all oscillators and other parameters are provided in Table 4.1

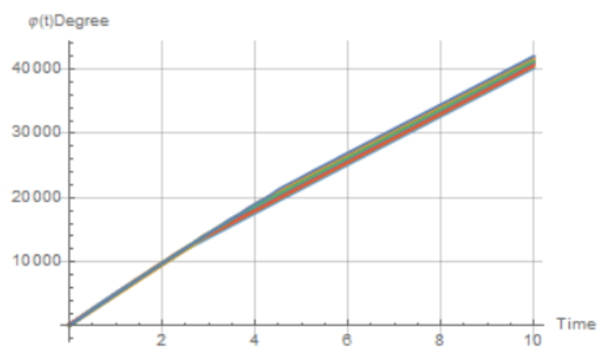

(a) $\varphi_{ij}(t)$ for final time $t_f = 10s$

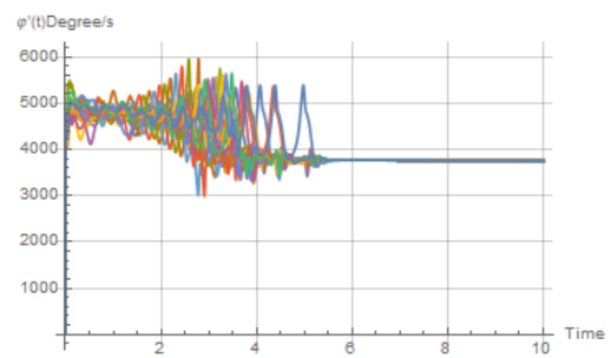

(b) $\dot{\varphi}_{ij}(t)$ for final time $t_f = 10s$

Figure 4.9: Evolution of the longitude angle (a) and its derivative (b) in the case where $m_B = m$. Other parameters are in Table 4.1

ments, where the base mass is lumped to m_B. All the oscillators exhibit slight variations from their initial polar positions.

The behaviour of the system in the two-dimensional lattice just presented has not undergone thorough analysis. The emergence of metachronal coordination has been induced via magnetic actuation in [18] [15]. Future work will focus on the nonlinear dynamic analysis of the model to be able to predict the emergence of coordinated patterns, which can then be used for the design of terrestrial locomotion systems.

4.4 Summary

The setup of the model simulation and the results can be summarized as follows:

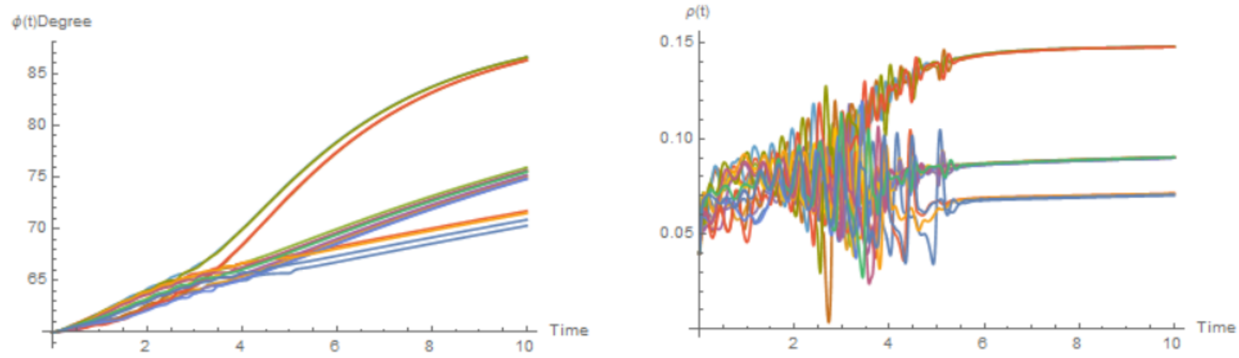

(a) $\phi_{ij}(t)$ for final time $t_f = 10s$ (b) $\rho_{ij}(t)$ the final time $t_f = 10s$

Figure 4.10: Evolution of co-latitude angle (left) and length of oscillators (right) in the case where $m_B = m$. Other parameters are in Table 4.1

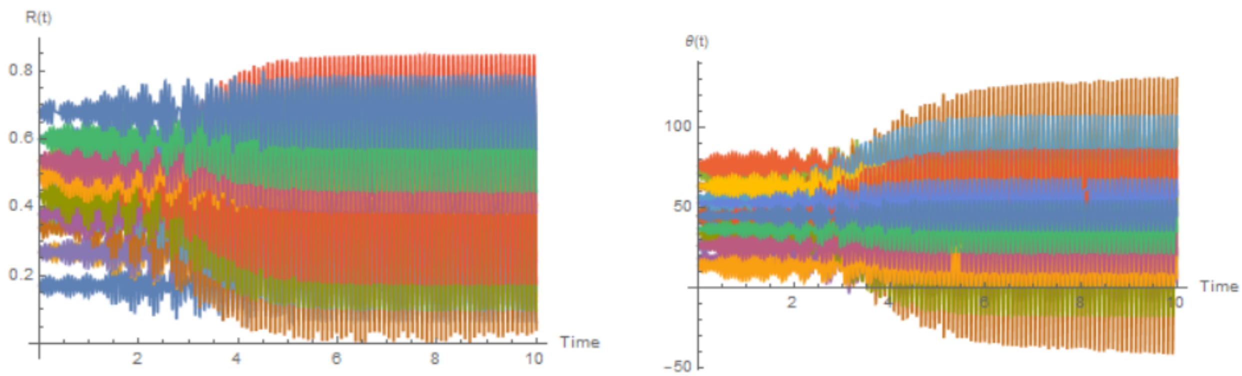

(a) $R_{ij}(t)$ for final time $t_f = 10s$ (b) $\theta_{ij}(t)$ for final time $t_f = 10s$

Figure 4.11: Evolution of the polar coordinates (R, θ) in the case where $m_B = 0.1m$. Other parameters are in Table 4.1

The parameter values, mainly leg length and mass, for the simulation are selected to achieve coordinated behaviour suitable for a miniature legged robot operating in a hazardous environment. To achieve this, damping values are set to be very low, especially along the longitude angle φ, and the stiffness values of the spring connecting to the wall K_w are higher than those connecting to adjacent oscillators K_{BC}.

The simulation considers an array with 8 oscillators, assuming a constant length ρ_0 for all oscillators. It is conducted under two scenarios: first, with the longitude angle φ distributed in a metachronal configuration with $\pi/4$ phase differences between adjacent oscillators; second, with φ randomly distributed in the interval $[0, 2\pi]$. In each scenario, synchronization emerges, with the system converging to a zero phase difference between adjacent oscillators. Furthermore, the simulation investigates the impact of mass concentration at the tip compared to the base, revealing that a higher mass concentration at the tip leads to a more rapid approach to a steady state.

However, the proposed model is flexible, allowing for adjustments in parameters such as leg length and co-latitude angle, as well as adjusting other parameters to achieve desired results.

Chapter 5

Conclusions and Future Work

Studying coordination patterns is crucial for terrestrial locomotion. Using rigid filaments in robotic leg construction, along with precise coordination, provides a practical approach for effective movement. This method requires proper actuation to induce the necessary coordinated patterns. Exploring coordination in robotic locomotion is significant for efficient performance, saving time and resources. It also enables robots to adapt to evolving environments and navigate complex terrains, enhancing their adaptability for various real-world scenarios.

This research focuses on bio-inspired robotics, particularly slender, flexible components inspired by cilia. When cilia are grouped together, they exhibit coordinated motions known as metachronal waves, which is relevant for locomotion. Extensive research has been conducted on the coordinated patterns of filaments connected by hydrodynamic interactions. Cilia, naturally adapted for hydrodynamic interaction, are ideal for aquatic locomotion. However, when considering terrestrial locomotion, the challenge arises in finding alternative mechanisms. Modelling for terrestrial locomotion has drawn inspiration from biology, where animals use cilia-like appendages for walking, exhibiting a metachronal waves. In some models, the coupling is achieved magnetically. Our focus, however, is on developing a lattice structure coupled by visco-elastic properties.

The thesis presents a mathematical model and simulation of two-dimensional arrays of coupled filaments in a lattice structure. The filaments are connected to a solid substrate in a lattice configuration, modelled as rigid bodies with lumped masses. The visco-elastic properties of the substrate are incorporated into springs and dampers connecting oscillators at attachment sites.

The dynamics of the system are derived using Euler-Lagrange equations. Simulations, conducted with Mathematica on an array of oscillators (8 in a row), explore coordination patterns with varying parameters. The equation of motion comprises five generalized coordinates, including the length of oscillators. However, for the purpose of simulation, we treat the length of each oscillator as constant.

The study considers two sets of initial conditions, defining different scenarios. In the first case, the initial condition is a metachronal state, in which contiguous pairs of oscillators start with the same longitude difference. In the second case, initial longitude angles are randomly distributed.

With both sets of initial conditions, namely metachronal and random, the simulated system's evolution exhibits convergence to a synchronized state, in which the phase of the longitude angle between pairs of contiguous oscillators is zero. This is true for different ratios of the lumped mass at the base of the oscillators over the lumped mass at the tip, and some different combination of visco-elastic coupling parameters between oscillators' attachment sites. Therefore, it seems that the linear coupling considered in the model acts as stabilizing negative feedback, regulating the phases of the longitudes to zero. Results are not comprehensive, since the simulation includes a limited number of cases; however, for the scenarios considered here, synchronization seems to be the emerging pattern. Further investigation in the nonlinear dynamics of the system is required to understand the parametric dependence of solutions and their classification.

In this work, elements at the boundary are connected to adjacent walls through elastic springs to prevent rigid-body modes. However, in future work, especially involving locomotion, rigid-body modes will need to be explicitly included.

For the scenarios simulated here, metachronal coordination did not emerge as a pattern via the basis. The nature and the topology of coupling elements could play a crucial role in inducing coordinated patterns. Ongoing work focuses on understanding the connection between visco-elastic coupling and the eventual emergence of coordinated stable states, with implications for the design of robots.

The preliminary results obtained in this thesis will serve as a guide for future work aimed at predicting emergent coordination patterns and quantitatively addressing wave propagation associated with synchronization and metachronal coordination. The final goal is designing mechanical systems for terrestrial locomotion, with the goal of enhancing miniature robot capabilities for navigating unstructured terrains.

The study of coordination patterns in two-dimensional distributions of oscillators is also the object of future work, with the goal of predicting and inducing wave-like motions in carpet-like structures. This class of applications is intended for robotic locomotion, but also for applications involving active materials and soft intelligent structures.

Chapter 6

Appendix

Figure permission letter for Figure 2.1 [30].

Hi Thakshila,

You can use the figure in your thesis. We have the newest version of the paper just published in the IEEE RA-L journal. Figure one is also used in that version but I don't think you need to get permission for it if you just use the old version of the paper in ArXiv as a reference.

Best,
Yasemin

Mathematica Code

The following script, written in the Wolfram Language and implemented in Mathematica 13, simulates the proposed cilia model.

Cilia with basal coupling : Lagrangian formulation with base in polar coordinates

Set parameters for simple numerical integration

In[ ]:=
```
ClearAll
```
Out[ ]=
```
ClearAll
```

In[1]:=
```
ρ0 = 1; (*Length of the cilium*)
ϕ0 = π / 3; (* Latitute angle of each cilium (see figure) *)
cρ = 1; (* Damping along the axis of the cilium *)
ci = 0.1; (*Damping in wall*)
cij = 0.1; (*Damping in basal coupling*)
cϕ = 1; (* Damping along the latitude m/mB *)
cφ = 0.1; (* Damping around the longitudinal direction *)
kρ = 20; (* Stiffness of the restoring term along the axis of the cilium *)
ki = 20; (* Stiffness of the ground springs *)
kij = 1; (* Stiffness of the basal coupling mB/m *)
L = 3; (* Initial distance among cilia bases,
corresponding to no restoring force at the base *)
m = 1; (* Mass (concentrated at the tip) *)
mB = m; (*Mass at the base*)
g = 9.81; (*gravity*)
kϕ = 2 m g L ; (* Stiffness of the restoring term to bring the cilium to ϕ0 *)
Fin = 10 Degree // N; (* Magnitude of the internal driving torque alonf λ *)
tf = 10; (* Final time for numerical integration *)
```

In[18]:=
```
nx = 1; (* Number of sites along x and y *)
ny = 2;
```

Define coordinates

Polar coordinates

In[ ]:=
```
(*
Xpolar[t_]=Table[{ToExpression["R"<>ToString[i]<>ToString[j]<>"[t]"],
   ToExpression["θ"<>ToString[i]<>ToString[j]<>"[t]"]},{i,nx},{j,ny}]
*)
```

```
In[20]:= R[t_] = Table[ToExpression["R" <> ToString[i] <> ToString[j] <> "[t]"], {i, nx}, {j, ny}]

Out[20]= {{R11[t], R12[t]}}

In[21]:= θ[t_] = Table[ToExpression["θ" <> ToString[i] <> ToString[j] <> "[t]"], {i, nx}, {j, ny}]

Out[21]= {{θ11[t], θ12[t]}}
```

Positions of the base sites in polar coordinates

```
In[22]:= X[t_] = Table[R[t][[i, j]] {Cos[θ[t][[i, j]]], Sin[θ[t][[i, j]]]}, {i, nx}, {j, ny}]

Out[22]= {{{Cos[θ11[t]] R11[t], R11[t] Sin[θ11[t]]}, {Cos[θ12[t]] R12[t], R12[t] Sin[θ12[t]]}}}
```

Radial coordinates of the cilia

```
In[23]:= ρ[t_] = Table[ToExpression["ρ" <> ToString[i] <> ToString[j] <> "[t]"], {i, nx}, {j, ny}]

Out[23]= {{ρ11[t], ρ12[t]}}
```

Angular spherical coordinates: latitude ϕ and longitude φ:

```
In[24]:= ϕ[t_] = Table[ToExpression["ϕ" <> ToString[i] <> ToString[j] <> "[t]"], {i, nx}, {j, ny}]

Out[24]= {{ϕ11[t], ϕ12[t]}}

In[25]:= φ[t_] = Table[ToExpression["φ" <> ToString[i] <> ToString[j] <> "[t]"], {i, nx}, {j, ny}]

Out[25]= {{φ11[t], φ12[t]}}
```

Generalized (Lagrangian) coordinates

```
In[26]:= q[t_] = Join[R[t], θ[t], ρ[t], ϕ[t], φ[t]] // Flatten

Out[26]= {R11[t], R12[t], θ11[t], θ12[t], ρ11[t], ρ12[t], ϕ11[t], ϕ12[t], φ11[t], φ12[t]}
```

Define the geometry

Position vector of the base

```
In[27]:= rB[t_] = Table[Join[X[t][[i, j]], {0}], {i, nx}, {j, ny}]

Out[27]= {{{Cos[θ11[t]] R11[t], R11[t] Sin[θ11[t]], 0},
           {Cos[θ12[t]] R12[t], R12[t] Sin[θ12[t]], 0}}}
```

Position vector of the tip

```
In[28]:= r[t_] = Table[rB[t][[i, j]] + ρ[t][[i, j]] {Sin[ϕ[t][[i, j]]] Cos[φ[t][[i, j]]],
            Sin[ϕ[t][[i, j]]] Sin[φ[t][[i, j]]], Cos[ϕ[t][[i, j]]]}, {i, nx}, {j, ny}]

Out[28]= {{{Cos[θ11[t]] R11[t] + Cos[φ11[t]] Sin[ϕ11[t]] ρ11[t],
            R11[t] Sin[θ11[t]] + Sin[ϕ11[t]] Sin[φ11[t]] ρ11[t], Cos[ϕ11[t]] ρ11[t]},
           {Cos[θ12[t]] R12[t] + Cos[φ12[t]] Sin[ϕ12[t]] ρ12[t],
            R12[t] Sin[θ12[t]] + Sin[ϕ12[t]] Sin[φ12[t]] ρ12[t], Cos[ϕ12[t]] ρ12[t]}}}
```

Lagrangian function and generalized external forces

Kinetic Energy

```
In[29]:= T = 1/2 Total[Flatten[Table[m D[r[t][[i, j]], t].D[r[t][[i, j]], t] +
          mB D[rB[t][[i, j]], t].D[rB[t][[i, j]], t], {i, nx}, {j, ny}]]]
```

Out[29]=
$$\frac{1}{2}\Big((\mathrm{Sin}[\theta 11[t]]\,R11'[t]+\mathrm{Cos}[\theta 11[t]]\,R11[t]\,\theta 11'[t])^2+(\mathrm{Cos}[\theta 11[t]]\,R11'[t]-R11[t]\,\mathrm{Sin}[\theta 11[t]]\,\theta 11'[t])^2+(\mathrm{Sin}[\theta 12[t]]\,R12'[t]+\mathrm{Cos}[\theta 12[t]]\,R12[t]\,\theta 12'[t])^2+(\mathrm{Cos}[\theta 12[t]]\,R12'[t]-R12[t]\,\mathrm{Sin}[\theta 12[t]]\,\theta 12'[t])^2+(\mathrm{Cos}[\phi 11[t]]\,\rho 11'[t]-\mathrm{Sin}[\phi 11[t]]\,\rho 11[t]\,\phi 11'[t])^2+(\mathrm{Sin}[\theta 11[t]]\,R11'[t]+\mathrm{Cos}[\theta 11[t]]\,R11[t]\,\theta 11'[t]+\mathrm{Sin}[\phi 11[t]]\,\mathrm{Sin}[\varphi 11[t]]\,\rho 11'[t]+\mathrm{Cos}[\phi 11[t]]\,\mathrm{Sin}[\varphi 11[t]]\,\rho 11[t]\,\phi 11'[t]+\mathrm{Cos}[\varphi 11[t]]\,\mathrm{Sin}[\phi 11[t]]\,\rho 11[t]\,\varphi 11'[t])^2+(\mathrm{Cos}[\theta 11[t]]\,R11'[t]-R11[t]\,\mathrm{Sin}[\theta 11[t]]\,\theta 11'[t]+\mathrm{Cos}[\varphi 11[t]]\,\mathrm{Sin}[\phi 11[t]]\,\rho 11'[t]+\mathrm{Cos}[\phi 11[t]]\,\mathrm{Cos}[\varphi 11[t]]\,\rho 11[t]\,\phi 11'[t]-\mathrm{Sin}[\phi 11[t]]\,\mathrm{Sin}[\varphi 11[t]]\,\rho 11[t]\,\varphi 11'[t])^2+(\mathrm{Cos}[\phi 12[t]]\,\rho 12'[t]-\mathrm{Sin}[\phi 12[t]]\,\rho 12[t]\,\phi 12'[t])^2+(\mathrm{Sin}[\theta 12[t]]\,R12'[t]+\mathrm{Cos}[\theta 12[t]]\,R12[t]\,\theta 12'[t]+\mathrm{Sin}[\phi 12[t]]\,\mathrm{Sin}[\varphi 12[t]]\,\rho 12'[t]+\mathrm{Cos}[\phi 12[t]]\,\mathrm{Sin}[\varphi 12[t]]\,\rho 12[t]\,\phi 12'[t]+\mathrm{Cos}[\varphi 12[t]]\,\mathrm{Sin}[\phi 12[t]]\,\rho 12[t]\,\varphi 12'[t])^2+(\mathrm{Cos}[\theta 12[t]]\,R12'[t]-R12[t]\,\mathrm{Sin}[\theta 12[t]]\,\theta 12'[t]+\mathrm{Cos}[\varphi 12[t]]\,\mathrm{Sin}[\phi 12[t]]\,\rho 12'[t]+\mathrm{Cos}[\phi 12[t]]\,\mathrm{Cos}[\varphi 12[t]]\,\rho 12[t]\,\phi 12'[t]-\mathrm{Sin}[\phi 12[t]]\,\mathrm{Sin}[\varphi 12[t]]\,\rho 12[t]\,\varphi 12'[t])^2\Big)$$

Mass matrix

```
In[30]:= MM = Table[D[T, q'[t][[i]], q'[t][[j]]], {i, Length[q[t]]}, {j, Length[q[t]]}];
```

Coupling for base sites: rectangular lattice

```
In[31]:= σ =
    Table[If[((Abs[j - i2] + Abs[i - i1]) < 2) && ((Abs[i - i1] == 1) || (Abs[j - i2] == 1)), 1, 0],
     {i, nx}, {j, ny}, {i1, nx}, {i2, ny}];
```

Potential energy: basal coupling

```
In[•]:= (*
Vij=Table[Sum[1/2 kij σ[[i,j,i1,i2]]
        (Sqrt[(X[t][[i,j]]-X[t][[i1,i2]]).(X[t][[i,j]]-X[t][[i1,i2]])]-L)^2,
      {i1,i,nx},{i2,j,ny}],{i,nx},{j,ny}]//Flatten//Total//Simplify
*)
```

```
In[32]:= Vij = Table[Sum[1/2 kij σ[[i, j, i1, i2]]
          ((rB[t][[i, j]] - rB[0][[i, j]]) - (rB[t][[i1, i2]] - rB[0][[i1, i2]])).
           ((rB[t][[i, j]] - rB[0][[i, j]]) - (rB[t][[i1, i2]] - rB[0][[i1, i2]])),
         {i1, i, nx}, {i2, j, ny}], {i, nx}, {j, ny}] // Flatten // Total
```

Out[32]=
$$\frac{1}{2}\Big((-\mathrm{Cos}[\theta 11[0]]\,R11[0]+\mathrm{Cos}[\theta 11[t]]\,R11[t]+\mathrm{Cos}[\theta 12[0]]\,R12[0]-\mathrm{Cos}[\theta 12[t]]\,R12[t])^2+(-R11[0]\,\mathrm{Sin}[\theta 11[0]]+R11[t]\,\mathrm{Sin}[\theta 11[t]]+R12[0]\,\mathrm{Sin}[\theta 12[0]]-R12[t]\,\mathrm{Sin}[\theta 12[t]])^2\Big)$$

Potential energy: ground springs

In[•]:=
```
(*
Vi=Sum[1/2 ki If[i==1||i==nx,(X[t][[i,j,2]]-X[0][[i,j,2]])^2,0],{i,nx},{j,ny}]+Sum[
    1/2 ki If[j==1||j==ny,(X[t][[i,j,1]]-X[0][[i,j,1]])^2,0],{i,nx},{j,ny}]//Simplify
*)
```

In[33]:=
```
Vi = Sum[1/2 ki If[i == 1 || i == nx || j == 1 || j == ny, (rB[t][[i, j]] - rB[0][[i, j]]).
    (rB[t][[i, j]] - rB[0][[i, j]]), 0], {i, nx}, {j, ny}] // Simplify
```

Out[33]= $10\left(R11[0]^2 - 2\,\mathrm{Cos}[\theta 11[0] - \theta 11[t]]\,R11[0]\times R11[t] + R11[t]^2 + R12[0]^2 - 2\,\mathrm{Cos}[\theta 12[0] - \theta 12[t]]\,R12[0]\times R12[t] + R12[t]^2\right)$

Potential energy : restoring spring in the ϕ direction

In[34]:=
```
Vϕ = Sum[1/2 kϕ (ϕ[t][[i, j]] - ϕ0)^2, {i, nx}, {j, ny}]
```

Out[34]= $29.43\left(-\frac{\pi}{3} + \phi 11[t]\right)^2 + 29.43\left(-\frac{\pi}{3} + \phi 12[t]\right)^2$

Potential energy : restoring spring in the ρ direction

In[35]:=
```
Vρ = Sum[1/2 kρ (ρ[t][[i, j]] - ρ0)^2, {i, nx}, {j, ny}]
```

Out[35]= $10\,(-1 + \rho 11[t])^2 + 10\,(-1 + \rho 12[t])^2$

Potential energy : gravity

In[36]:=
```
Vg =
 Sum[m g L ((r[t][[i, j]] /. {ϕ[t][[i, j]] -> 0}) - r[t][[i, j]]).{0, 0, 1}, {i, nx}, {j, ny}]
```

Out[36]= $29.43\,(\rho 11[t] - \mathrm{Cos}[\phi 11[t]]\,\rho 11[t]) + 29.43\,(\rho 12[t] - \mathrm{Cos}[\phi 12[t]]\,\rho 12[t])$

Viscous damping in ρ, ϕ, and φ directions (use Rayleigh’s potential)

In[37]:=
```
Rρ = Sum[1/2 cρ (ρ'[t][[i, j]])^2, {i, nx}, {j, ny}]
Rϕ = Sum[1/2 cϕ (ϕ'[t][[i, j]])^2, {i, nx}, {j, ny}]
Rφ = Sum[1/2 cφ (φ'[t][[i, j]])^2, {i, nx}, {j, ny}]
```

Out[37]= $\frac{1}{2}\rho 11'[t]^2 + \frac{1}{2}\rho 12'[t]^2$

Out[38]= $\frac{1}{2}\phi 11'[t]^2 + \frac{1}{2}\phi 12'[t]^2$

Out[39]= $0.05\,\varphi 11'[t]^2 + 0.05\,\varphi 12'[t]^2$

Viscous damping in basal coupling

```
In[42]:= RB = Sum[1/2 ci If[i == 1 || i == nx || j == 1 || j == ny,
            (D[rB[t][[i, j]], t]).(D[rB[t][[i, j]], t])], {i, nx}, {j, ny}]

         RBC = Table[Sum[1/2 cij σ[[i, j, i1, i2]] ((D[rB[t][[i, j]], t]) - (D[rB[t][[i1, i2]], t])).
                 ((D[rB[t][[i, j]], t]) - (D[rB[t][[i1, i2]], t])),
               {i1, i, nx}, {i2, j, ny}], {i, nx}, {j, ny}] // Flatten // Total

Out[42]= 0.05 ((Sin[θ11[t]] R11′[t] + Cos[θ11[t]] R11[t] θ11′[t])^2 +
            (Cos[θ11[t]] R11′[t] - R11[t] Sin[θ11[t]] θ11′[t])^2) +
          0.05 ((Sin[θ12[t]] R12′[t] + Cos[θ12[t]] R12[t] θ12′[t])^2 +
            (Cos[θ12[t]] R12′[t] - R12[t] Sin[θ12[t]] θ12′[t])^2)

Out[43]= 0. +
          0.05 ((Sin[θ11[t]] R11′[t] - Sin[θ12[t]] R12′[t] + Cos[θ11[t]] R11[t] θ11′[t] - Cos[θ12[t]]
                R12[t] θ12′[t])^2 + (Cos[θ11[t]] R11′[t] - Cos[θ12[t]] R12′[t] -
               R11[t] Sin[θ11[t]] θ11′[t] + R12[t] Sin[θ12[t]] θ12′[t])^2)
```

Internal forces acting only along φ

```
In[44]:= fin = Join[Table[0, Length[Flatten[R[t]]]],
           Table[0, Length[Flatten[θ[t]]]], Table[0, Length[Flatten[ρ[t]]]],
           Table[0, Length[Flatten[ϕ[t]]]], Fin Table[1, Length[Flatten[φ[t]]]]]

Out[44]= {0, 0, 0, 0, 0, 0, 0, 0, 0.174533, 0.174533}
```

Lagrangian function

In[45]:=
```
Lagr = T - (Vi + Vij + Vϕ + Vρ + Vg)
```

Out[45]=
```
-10 (R11[0]^2 - 2 Cos[θ11[0] - θ11[t]] R11[0] × R11[t] +
    R11[t]^2 + R12[0]^2 - 2 Cos[θ12[0] - θ12[t]] R12[0] × R12[t] + R12[t]^2) +
 1/2 (-(-Cos[θ11[0]] R11[0] + Cos[θ11[t]] R11[t] + Cos[θ12[0]] R12[0] - Cos[θ12[t]] R12[t])^2 -
    (-R11[0] Sin[θ11[0]] + R11[t] Sin[θ11[t]] + R12[0] Sin[θ12[0]] - R12[t] Sin[θ12[t]])^2) -
 10 (-1 + ρ11[t])^2 - 29.43 (ρ11[t] - Cos[ϕ11[t]] ρ11[t]) - 10 (-1 + ρ12[t])^2 -
 29.43 (ρ12[t] - Cos[ϕ12[t]] ρ12[t]) -
 29.43 (-π/3 + ϕ11[t])^2 - 29.43 (-π/3 + ϕ12[t])^2 +
 1/2 ((Sin[θ11[t]] R11′[t] + Cos[θ11[t]] R11[t] θ11′[t])^2 +
    (Cos[θ11[t]] R11′[t] - R11[t] Sin[θ11[t]] θ11′[t])^2 +
    (Sin[θ12[t]] R12′[t] + Cos[θ12[t]] R12[t] θ12′[t])^2 +
    (Cos[θ12[t]] R12′[t] - R12[t] Sin[θ12[t]] θ12′[t])^2 +
    (Cos[ϕ11[t]] ρ11′[t] - Sin[ϕ11[t]] ρ11[t] ϕ11′[t])^2 +
    (Sin[θ11[t]] R11′[t] + Cos[θ11[t]] R11[t] θ11′[t] + Sin[ϕ11[t]] Sin[φ11[t]] ρ11′[t] +
       Cos[ϕ11[t]] Sin[φ11[t]] ρ11[t] ϕ11′[t] + Cos[φ11[t]] Sin[ϕ11[t]] ρ11[t] φ11′[t])^2 +
    (Cos[θ11[t]] R11′[t] - R11[t] Sin[θ11[t]] θ11′[t] + Cos[φ11[t]] Sin[ϕ11[t]] ρ11′[t] +
       Cos[ϕ11[t]] Cos[φ11[t]] ρ11[t] ϕ11′[t] - Sin[ϕ11[t]] Sin[φ11[t]] ρ11[t] φ11′[t])^2 +
    (Cos[ϕ12[t]] ρ12′[t] - Sin[ϕ12[t]] ρ12[t] ϕ12′[t])^2 +
    (Sin[θ12[t]] R12′[t] + Cos[θ12[t]] R12[t] θ12′[t] + Sin[ϕ12[t]] Sin[φ12[t]] ρ12′[t] +
       Cos[ϕ12[t]] Sin[φ12[t]] ρ12[t] ϕ12′[t] + Cos[φ12[t]] Sin[ϕ12[t]] ρ12[t] φ12′[t])^2 +
    (Cos[θ12[t]] R12′[t] - R12[t] Sin[θ12[t]] θ12′[t] + Cos[φ12[t]] Sin[ϕ12[t]] ρ12′[t] +
       Cos[ϕ12[t]] Cos[φ12[t]] ρ12[t] ϕ12′[t] - Sin[ϕ12[t]] Sin[φ12[t]] ρ12[t] φ12′[t])^2)
```

Governing equations and initial conditions

Euler - Lagrange equations:

In[46]:=
```
eqs = Table[D[D[Lagr, q'[t][[i]]], t] - D[Lagr, q[t][[i]]] +
   D[RB + RBC + Rρ + Rϕ + Rφ, q'[t][[i]]] - fin[[i]], {i, Length[q[t]]}]
```

Out[46]=
```
{ ⋯ 1 ⋯ }
large output    show less    show more    show all    set size limit...
```

Initial conditions: the base sites are distributed on a rectangular lattice according to the parameters above, expressed in polar coordinates (R, θ). The initial length of each cilium is ρ_0; the initial latitude is ϕ_0; the initial longitude φ_0 is randomly distributed in {0, 2 π}:

In[∘]:=
```
(*
ic=Join[q[0]-Join[Table[{i,j},{i,0,(nx-1) L,L},{j,0,(ny-1) L,L}]//Flatten[#,2]&,
    ρ0 Table[1,nx ny],ϕ0 Table[1,nx ny]+RandomReal[{ϕ0-π/6,ϕ0+π/6},nx ny],
    RandomReal[{0,2π},nx ny]],q'[0]]
*)
```

In[47]:=
```
icCoeff = Join[Table[Sqrt[Total[{i, j}^2]], {i, L, nx L, L}, {j, L, ny L, L}] // Flatten,
   Table[If[(i != 0) && (j != 0), ArcTan[i, j], 0], {i, L, nx L, L}, {j, L, ny L, L}] // Flatten,
   ρ0 Table[1, nx ny], ϕ0 Table[1, nx ny], RandomReal[{0, 2 π}, nx ny]];
ic = Join[q[0] - icCoeff, q'[0]];
```

In[∘]:=
```
icCoeff
```

Out[∘]= $\left\{3\sqrt{2},\ 3\sqrt{5},\ \frac{\pi}{4},\ \text{ArcTan}[2],\ 1,\ 1,\ \frac{\pi}{4},\ \frac{\pi}{4},\ 6.16207,\ 4.2928\right\}$

Numerical integration

Using the built - in numerical integration

In[49]:=
```
qs[t_] = First[NDSolve[Thread[Join[(eqs //. Thread[q[0] -> icCoeff]), ic] == 0],
   q[t], {t, 0, tf}, Method → {"EquationSimplification" → "Residual"}]]
```

Out[49]=
```
{R11[t] → InterpolatingFunction[ Domain: {{0., 10.}} Output: scalar ][t],
 R12[t] → InterpolatingFunction[ Domain: {{0., 10.}} Output: scalar ][t],
 θ11[t] → InterpolatingFunction[ Domain: {{0., 10.}} Output: scalar ][t],
 θ12[t] → InterpolatingFunction[ Domain: {{0., 10.}} Output: scalar ][t],
 ρ11[t] → InterpolatingFunction[ Domain: {{0., 10.}} Output: scalar ][t],
 ρ12[t] → InterpolatingFunction[ Domain: {{0., 10.}} Output: scalar ][t],
 ϕ11[t] → InterpolatingFunction[ Domain: {{0., 10.}} Output: scalar ][t],
 ϕ12[t] → InterpolatingFunction[ Domain: {{0., 10.}} Output: scalar ][t],
 φ11[t] → InterpolatingFunction[ Domain: {{0., 10.}} Output: scalar ][t],
 φ12[t] → InterpolatingFunction[ Domain: {{0., 10.}} Output: scalar ][t]}
```

Plots

In[50]:=
```
ParametricPlot3D[
 Flatten[Table[Join[X[t][[i, j]], {0}] /. qs[t], {i, nx}, {j, ny}], 1], {t, 0, tf}]
```

Out[50]=

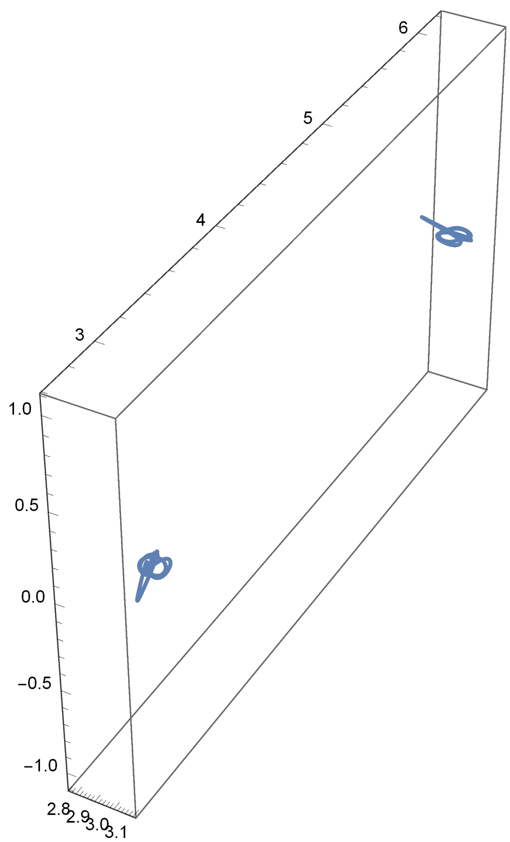

In[51]:=
```
ParametricPlot3D[Flatten[Table[Join[X[t][[i, j]], {0}] /. qs[t], {i, nx}, {j, ny}], 1],
 {t, 0, tf}, AxesLabel → {"X", "Y", "Z"}, (*Label the axes*)
 PlotLabel → "Cilia Motion", (*Add a title*) Boxed → False,
 (*Turn off the box around the plot*) ViewPoint → {2, -2, 1}]
```

Out[51]=

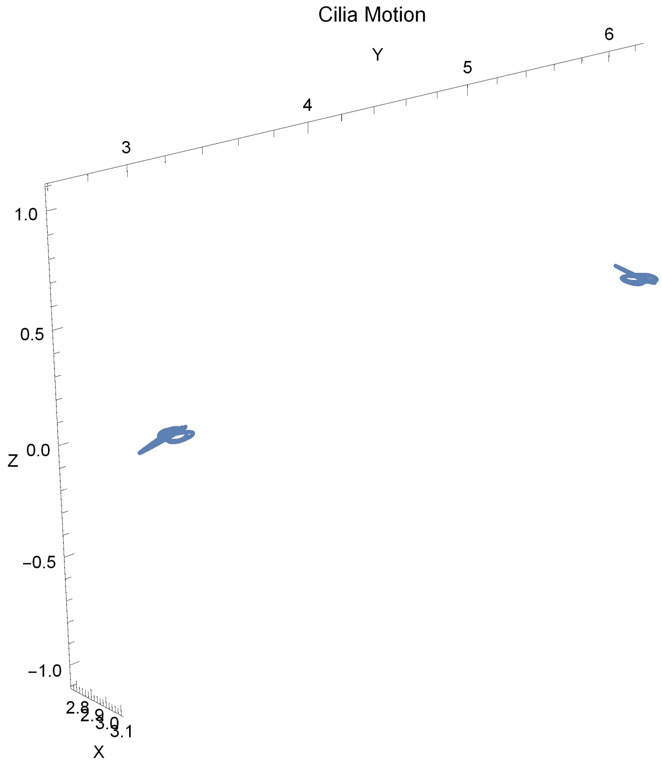

In[52]:=
```
Plot[Evaluate[(φ[t] /. qs[t]) / Degree], {t, 0, tf}, PlotRange -> All]
```

Out[52]=

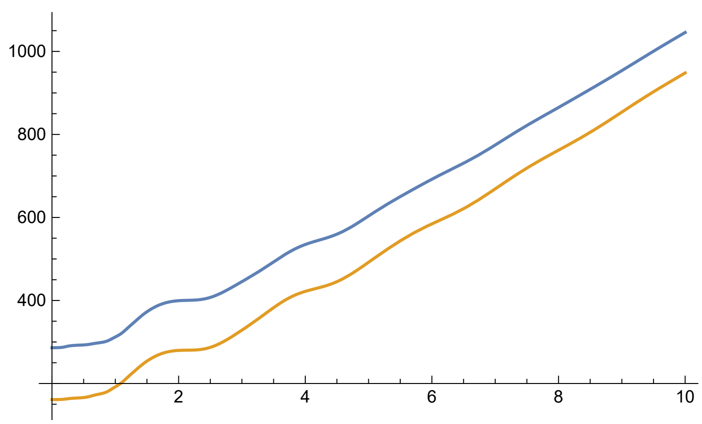

Data for plots

In[53]:=
```
dataB = Flatten[Table[rB[t][[i, j]] /. qs[t], {i, nx}, {j, ny}, {t, 0, tf, tf / 50}], 1];
```

In[54]:=
```
dataT = Flatten[Table[r[t][[i, j]] /. qs[t], {i, nx}, {j, ny}, {t, 0, tf, tf / 50}], 1];
```

Trajectories of the base

```
In[55]:= ListLinePlot3D[dataB, PlotRange -> {{L / 2, nx L + L / 2}, {L / 2, ny L + L / 2}, {-.1, .1}}]

Out[55]= ListLinePlot3D[
  {{{3., 3., 0}, {3.05856, 2.77197, 0}, {2.96269, 3.00018, 0}, {3.00025, 2.95147, 0},
    {2.96157, 3.08008, 0}, {2.96662, 3.08892, 0}, {2.96836, 3.07373, 0},
    {2.97523, 3.02442, 0}, {3.00412, 2.96403, 0}, {3.04532, 2.93761, 0},
    {3.07075, 2.96382, 0}, {3.06754, 3.01993, 0}, {3.04638, 3.06507, 0},
    {3.02114, 3.06805, 0}, {3.00309, 3.03488, 0}, {2.99503, 2.99578, 0},
    {2.99382, 2.97706, 0}, {2.99452, 2.98998, 0}, {2.98841, 3.02647, 0},
    {2.96987, 3.05891, 0}, {2.94775, 3.05956, 0}, {2.93758, 3.02639, 0},
    {2.94531, 2.98316, 0}, {2.96365, 2.95686, 0}, {2.97869, 2.95569, 0},
    {2.98339, 2.96632, 0}, {2.98434, 2.97182, 0}, {2.99164, 2.96693, 0},
    {3.00817, 2.95682, 0}, {3.02974, 2.9499, 0}, {3.04956, 2.95332, 0}, {3.06129, 2.96955, 0},
    {3.0616, 2.99417, 0}, {3.05243, 3.01822, 0}, {3.04008, 3.03469, 0}, {3.03012, 3.04351, 0},
    {3.02221, 3.04931, 0}, {3.01116, 3.05476, 0}, {2.99364, 3.05768, 0}, {2.97203, 3.0545, 0},
    {2.95216, 3.04407, 0}, {2.93891, 3.02776, 0}, {2.93431, 3.00795, 0},
    {2.93794, 2.98721, 0}, {2.94776, 2.96823, 0}, {2.96101, 2.95302, 0}, {2.97589, 2.9422, 0},
    {2.99248, 2.93593, 0}, {3.01148, 2.93529, 0}, {3.03179, 2.9418, 0}, {3.05014, 2.9556, 0}},
   {{3., 6., 0}, {2.77778, 6.07751, 0}, {3.01519, 6.01063, 0}, {2.95642, 6.02105, 0},
    {3.08618, 5.99411, 0}, {3.09056, 5.99718, 0}, {3.07455, 6.00531, 0},
    {3.02773, 6.01767, 0}, {2.96303, 6.01117, 0}, {2.92443, 5.97682, 0},
    {2.94061, 5.93576, 0}, {2.99614, 5.91341, 0}, {3.04756, 5.92018, 0}, {3.0592, 5.95439, 0},
    {3.03173, 5.99487, 0}, {2.99408, 6.01889, 0}, {2.97608, 6.01835, 0},
    {2.99279, 6.00175, 0}, {3.03629, 5.99149, 0}, {3.07476, 6.00588, 0},
    {3.07688, 6.03922, 0}, {3.04089, 6.06856, 0}, {2.99329, 6.07431, 0},
    {2.96417, 6.05514, 0}, {2.96368, 6.02879, 0}, {2.97725, 6.014, 0}, {2.98298, 6.01334, 0},
    {2.97098, 6.01563, 0}, {2.94807, 6.00818, 0}, {2.93084, 5.98649, 0},
    {2.93331, 5.95771, 0}, {2.95669, 5.93554, 0}, {2.98915, 5.92997, 0},
    {3.01556, 5.93996, 0}, {3.02888, 5.95529, 0}, {3.03392, 5.96628, 0},
    {3.04036, 5.97219, 0}, {3.05243, 5.98013, 0}, {3.06528, 5.99679, 0},
    {3.06978, 6.02185, 0}, {3.06006, 6.04791, 0}, {3.0378, 6.06585, 0},
    {3.01059, 6.07093, 0}, {2.98641, 6.06511, 0}, {2.96867, 6.05427, 0},
    {2.95548, 6.04283, 0}, {2.94355, 6.03046, 0}, {2.93283, 6.01373, 0},
    {2.92741, 5.99088, 0}, {2.93209, 5.96488, 0}, {2.9482, 5.94216, 0}}},
  PlotRange → {{3/2, 9/2}, {3/2, 15/2}, {-0.1, 0.1}}]
```

Animation with discrete time sampling

Bibliography

[1] Seong Chiun Lim and Gik Hong Yeap. "The locomotion of bipedal walking robot with six degree of freedom". In: *Procedia Engineering* 41 (2012), pp. 8–14.

[2] Fred Delcomyn. "Biologically inspired robots". In: *Bioinspiration and Robotics Walking and Climbing Robots*. IntechOpen, 2007.

[3] Abdulkareem Sh Mahdi Al-Obaidi Al et al. "Embedded design and implementation of mobile robot for surveillance applications". In: *Indonesian Journal of Science and Technology* 6.2 (2021), pp. 427–440.

[4] P Thanh Tran-Ngoc et al. "A robotic leg inspired from an insect leg". In: *Bioinspiration & Biomimetics* 17.5 (2022), p. 056008.

[5] Yifeng Gong et al. "Legged robots for object manipulation: A review". In: *Frontiers in Mechanical Engineering* 9 (2023), p. 1142421.

[6] Garth Chapman. "The hydrostatic skeleton in the invertebrates". In: *Biological reviews* 33.3 (1958), pp. 338–371.

[7] Thomas Niedermayer, Bruno Eckhardt, and Peter Lenz. "Synchronization, phase locking, and metachronal wave formation in ciliary chains". In: *Chaos: An Interdisciplinary Journal of Nonlinear Science* 18.3 (2008), p. 037128.

[8] Davide Spinello. "Coordination in coupled arrays of stiff filaments—modelling and simulation". In: *Mathematics* 8.8 (2020), p. 1282.

[9] Weicheng Huang, Mingchao Liu, and K Jimmy Hsia. "Modeling of magnetic cilia carpet robots using discrete differential geometry formulation". In: *Extreme Mechanics Letters* 59 (2023), pp. 101–967.

[10] Anil Antony Sequeira et al. "Biologically Inspired Robots into a New Dimension-A Review". In: *International Journal of Automation, Mechatronics & Robotics* 3.1 (2016), pp. 106–116.

[11] Shinya Aoi et al. "Adaptive control strategies for interlimb coordination in legged robots: a review". In: *Frontiers in Neurorobotics* 11 (2017), p. 39.

[12] Jihun Han and Charles S Peskin. “Spontaneous oscillation and fluid–structure interaction of cilia”. In: *Proceedings of the National Academy of Sciences* 115.17 (2018), pp. 4417–4422.

[13] Benjamin M Friedrich and Frank Jülicher. “Flagellar synchronization independent of hydrodynamic interactions”. In: *Physical Review Letters* 109.13 (2012), p. 138102.

[14] Jens Elgeti and Gerhard Gompper. “Emergence of metachronal waves in cilia arrays”. In: *Proceedings of the National Academy of Sciences* 110.12 (2013), pp. 4470–4475.

[15] Hongri Gu et al. “Magnetic cilia carpets with programmable metachronal waves”. In: *Nature Communications* 11.1 (2020), p. 2637.

[16] David Wettergreen. “Robotic walking in natural terrain”. In: *Gait Planning and Behavior Based Control for Statically-Stable Walking Robots: D. Wettergreen–Pittsburgh PA* (1995).

[17] Nariya Uchida and Ramin Golestanian. “Synchronization and collective dynamics in a carpet of microfluidic rotors”. In: *Physical Review Letters* 104.17 (2010), p. 178103.

[18] Zhiwei Cui et al. “Miniaturized metachronal magnetic artificial cilia”. In: *Proceedings of the National Academy of Sciences* 120.35 (2023), e2304519120.

[19] Jun He and Feng Gao. “Mechanism, actuation, perception, and control of highly dynamic multilegged robots: A review”. In: *Chinese Journal of Mechanical Engineering* 33.1 (2020), pp. 1–30.

[20] Robert Bogue. “Search and rescue and disaster relief robots: has their time finally come?” In: *Industrial Robot: An International Journal* 43.2 (2016), pp. 138–143.

[21] Gerardo Diaz-Arango et al. “Homotopy path planning for terrestrial robots using spherical algorithm”. In: *IEEE Transactions on Automation Science and Engineering* 15.2 (2017), pp. 567–585.

[22] Woojin Chung and Karl Iagnemma. “Wheeled robots”. In: *Springer Handbook of Robotics* (2016), pp. 575–594.

[23] Jing Liu, Min Tan, and Xiaoguang Zhao. “Legged robots—an overview”. In: *Transactions of the Institute of Measurement and Control* 29.2 (2007), pp. 185–202.

[24] Pierre-Brice Wieber, Russ Tedrake, and Scott Kuindersma. “Modeling and control of legged robots”. In: *Springer Handbook of Robotics*. Springer, 2016, pp. 1203–1234.

[25] Mattias Wahde and Jimmy Pettersson. “A brief review of bipedal robotics research”. In: *Proceedings of the 8th UK Mechatronics Forum International Conference (Mechatronics 2002)*. 2002, pp. 480–488.

[26] Lingxuan Zhao et al. "System design and balance control of a novel electrically-driven wheel-legged humanoid robot". In: *2021 IEEE International Conference on Unmanned Systems (ICUS)*. IEEE. 2021, pp. 742–747.

[27] Xiao-Qiao Wang and Ghim Wei Ho. "Design of untethered soft material micromachine for life-like locomotion". In: *Materials Today* 53 (2022), pp. 197–216.

[28] Daniela Rus and Michael T Tolley. "Design, fabrication and control of soft robots". In: *Nature* 521.7553 (2015), pp. 467–475.

[29] Chelsea Shan Xian Ng et al. "Locomotion of miniature soft robots". In: *Advanced Materials* 33.19 (2021), p. 2003558.

[30] Abu Nayem Md Asraf Siddiquee, Benjamin Colfer, and Yasemin Ozkan-Aydin. "Design of soft, modular appendages for a bio-inspired multi-legged terrestrial robot". In: *arXiv preprint arXiv:2304.04293* (2023).

[31] Ruomeng Xu and Qingsong Xu. "Design of a bio-inspired untethered soft octopodal robot driven by magnetic field". In: *Biomimetics* 8.3 (2023), p. 269.

[32] D. Wettergreen, H. Pangels, and J. Bares. "Behavior-based gait execution for the Dante II walking robot". In: *Proceedings 1995 IEEE/RSJ International Conference on Intelligent Robots and Systems. Human Robot Interaction and Cooperative Robots*. Vol. 3. 1995, 274–279 vol.3. DOI: 10.1109/IROS.1995.525895.

[33] Timothy Bretl and Sanjay Lall. "Testing static equilibrium for legged robots". In: *IEEE Transactions on Robotics* 24.4 (2008), pp. 794–807.

[34] H Benjamin Brown and Yangsheng Xu. "A single-wheel, gyroscopically stabilized robot". In: *Proceedings of IEEE International Conference on Robotics and Automation*. Vol. 4. IEEE. 1996, pp. 3658–3663.

[35] Baxi Chong et al. "A general locomotion control framework for multi-legged locomotors". In: *Bioinspiration & Biomimetics* 17.4 (2022), p. 046015.

[36] William Gilpin, Matthew Storm Bull, and Manu Prakash. "The multiscale physics of cilia and flagella". In: *Nature Reviews Physics* 2.2 (2020), pp. 74–88.

[37] Thomas Heuser et al. "The dynein regulatory complex is the nexin link and a major regulatory node in cilia and flagella". In: *Journal of Cell Biology* 187.6 (2009), pp. 921–933.

[38] Xiaoguang Dong et al. "Bioinspired cilia arrays with programmable nonreciprocal motion and metachronal coordination". In: *Science Advances* 6.45 (2020), eabc9323.

[39] Mike Adams. “The primary cilium: An orphan organelle finds a home”. In: *Nature Education* 3.9 (2010), p. 54.

[40] Yong Ha Youn and Young-Goo Han. “Primary cilia in brain development and diseases”. In: *The American Journal of Pathology* 188.1 (2018), pp. 11–22.

[41] Kelimar Diaz et al. “A minimal robophysical model of quadriflagellate self-propulsion”. In: *Bioinspiration & Biomimetics* 16.6 (2021), p. 066001.

[42] Ylona Collard, Galien Grosjean, and Nicolas Vandewalle. “Magnetically powered metachronal waves induce locomotion in self-assemblies”. In: *Communications Physics* 3.1 (2020), p. 112.

[43] Leonard Meirovitch. *Fundamentals of Vibrations*. Waveland Press, 2010.

[44] Mehrzad Tabatabaian et al. *Engineering Systems Dynamics Modelling, Simulation, and Design*. British Columbia Institute of Technology, 2021.

[45] George B Arfken and Hans-Jurgen Weber. “Mathematical methods for physicists”. In: *Academic Press Orlando, FL* (1972).